



NUMERICAL DESIGN OF UAV WITH COANDA EFFECT

İREM TELLİ

SEPTEMBER 2022

ÇANKAYA UNIVERSITY

GRADUATE SCHOOL OF NATURAL AND APPLIED SCIENCES

DEPARTMENT OF MECHATRONICS ENGINEERING

MASTER'S THESIS IN

MECHATRONICS ENGINEERING



NUMERICAL DESIGN OF UAV with COANDA EFFECT

İREM TELLİ

SEPTEMBER 2022

ABSTRACT

NUMERICAL DESIGN OF UAV WITH COANDA EFFECT

TELLİ, İrem

Master of Science in Mechatronics Engineering

Supervisor: Assoc. Prof. Dr. Ece AYLI

September 2022, 71 pages

With the development of technology, different aircraft are needed in aviation applications. Models of unmanned aerial vehicles (UAVs) are becoming more functional. Single-engine VTOL UAVs are widely used in the defense sector due to their high engine efficiency. Numerous studies have been conducted on increasing the flight performance of UAVs. Henry Coanda found the Coanda effect, a flow phenomenon. Coanda air surfaces increase the lifting force when used on UAV models.

This thesis aims to create surface parameters that will produce the Coanda effect and to numerically simulate these parameters in order to give VTOL-capable UAVs a flight advantage. By researching the history of aviation and UAVs, UAV designs that can move VTOL and use the Coanda effect are examined. The Coanda effect is examined. The structural design is explained.

The surface parameters on which the Coanda effect will be active have been determined. A mechanical model was drawn accordingly. The radius of curvature V_1 parameter was determined as the arc length V_2 parameter, which determines the direction of the flow after leaving the surface.

Turbulence modeling and boundary conditions are mentioned. Terms affecting aerodynamic performance are explained. Simulations were developed to improve these values' performance. In the numerical method part, Navier-Stokes equations are solved to examine the effects of parameters on aerodynamic performance using the

finite volume method. As the verification method, Bernoulli's equation and the equation estimating the separation angle found in the literature were used. As a result of the analysis, the optimum surface parameters were decided.

Keywords: UAV, Coanda Effect, Coanda Effect UAV, VTOL, Aerodynamics



ÖZ

COANDA ETKİLİ İHA SAYISAL TASARIMI

TELLİ, İrem

Mekatronik Mühendisliği Yüksek Lisans

Danışman: Assoc. Prof. Dr. Ece AYLI

Eylül 2022, 71 sayfa

Son zamanlarda teknolojinin gelişmesi ile birlikte havacılık uygulamalarında farklı hava araçlarına ihtiyaç duyulmaktadır. İşlevsellik bakımından İnsansız Hava Aracı (İHA) modelleri gelişmektedir. Motor verimliliği açısından, tek motorlu dikey iniş kalkış (VTOL) yapabilen İHA'lar savunma sektöründe sıklıkla kullanılmaktadır. İHA'ların uçuş performansının artırılması üzerine çok sayıda araştırma yapılmıştır. Coanda etkisi temellerini Henry Coanda'nın atmış olduğu bir akış fenomenidir. İHA modelleri üzerinde Coanda hava yüzeyi kullanılması kaldırma kuvvetini büyük ölçüde arttırmaktadır.

Bu tezde, dikey iniş kalkış (VTOL) yapabilen İHA'lara uçuş avantajı sağlaması için Coanda etkisi yaratacak yüzey parametrelerinin oluşturulması ve bu parametrelerin numerik olarak simüle edilmesi amaçlanmıştır. Havacılık ve İHA tarihleri araştırılarak, VTOL hareket edebilen ve Coanda etkisi kullanılan İHA tasarımları incelenmiştir. Coanda etkisi incelenmiş, yapısal tasarım aşamaları anlatılmıştır.

Model üzerinde Coanda etkisinin aktif olabileceği yüzeyi oluşturmak için parametreler belirlenmiş ve buna uygun olarak mekanik modeli çizilmiştir. Kavisli yüzeyi oluşturan radyus değişkenleri V_1 parametreleri olarak belirlenmiştir. Akışın kavisli yüzeyden sonra yönünü belirleyen yay uzunluğu değişkenleri ise V_2 parametreleri olarak

belirlenmiştir. Türbülans modellemesi ve sınır koşullarından bahsedilmiştir. Aerodinamik performansı etkileyen terimler açıklanmıştır. Bu değerlerin performansı arttırmasına yönelik simülasyonlar oluşturulmuştur. Numerik metod kısmında, sonlu hacim yöntemi kullanılarak parametrelerin aerodinamik performansa etkilerini incelemek için Navier-Stokes denklemleri çözdürülmüştür. Numerik sonuçların deneyselliğini kontrol etmek için Bernoulli denklemi ile karşılaştırılmıştır. Diğer doğrulama yöntemi olarak, literatürde bulunan yüzeyden akışın ayrılma açısını öngören ampirik denklem kullanılmıştır. Coanda etkisi oluşturan eğrilik yarıçapı ve yay uzunluğu parametreleri analizlere göre kıyaslanmış, optimum yüzey parametrelerine karar verilmiştir.

Anahtar Kelimeler: İHA, Coanda Etkisi, Coanda Etkili İHA, VTOL, Aerodinamik

ACKNOWLEDGEMENT

I would like to express my sincere gratitude to my parents for their support and sacrifice to me. Your memories would ever shine in my mind.

Special thanks to my supervisor Assoc. Prof. Dr. Ece AYLI for the excellent guidance and providing me with an excellent atmosphere to conduct this research. I would also like to thank Dr. Eyüp KOÇAK for helping me with all the subjects I consulted and did not leave my questions unanswered during this thesis work. My special gratitude also goes to the rest of the thesis committee for the encouragement and insightful comments.

TABLE OF CONTENTS

STATEMENT OF NONPLAGIARISM	iii
ABSTRACT	iv
ÖZ	vi
ACKNOWLEDGEMENT	viii
TABLE OF CONTENTS	ix
LIST OF TABLES	xi
LIST OF FIGURES	xii
LIST OF SYMBOLS AND ABBREVIATIONS	xiv
CHAPTER I: INTRODUCTION	1
1.1. HISTORY OF AVIATION	1
1.2. UNMANNED AERIAL VEHICLE	5
1.3. COANDA EFFECT	6
1.4. COANDA EFFECT VTOL UAV	8
1.4.1. Coanda UAV Background	10
1.4.2. Coanda Effect UAV Theoretical Background	13
1.5. AIM OF THESIS	16
CHAPTER II: MECHANICAL DESIGN	17
CHAPTER III: NUMERICAL METHODOLOGY	22
3.1. PHYSICAL AND MATHEMATICAL EXPRESSION OF TURBULENCE 22	
3.1.1. Physical Expression of turbulence	22
3.1.2. Mathematical Expression of Turbulence	22
3.1.3. Modeling of Turbulence and Numerical Approaches	23
3.1.4. The SST k- ω Turbulence Model	25
3.2. AERODYNAMICS PERFORMANCE INVESTIGATIONS	26
3.3. NUMERICAL SET-UP	29
3.3.1. Test Matrix	29
3.3.2. Boundary Condition	30
3.3.3. Force Calculation	31
3.3.4. Structural Design	33

3.3.5. Mesh Independency Study	37
3.3.6. Validation Study	38
CHAPTER IV: RESULTS	41
4.1. INVESTIGATION OF THE V_1 EFFECT ON PERFORMANCE	42
4.1.2. Velocity Contours of V_1 Parameters.....	44
4.2. INVESTIGATION OF THE V_2 EFFECT ON PERFORMANCE	46
4.2.1. Velocity Contours of V_2 Parameters.....	47
4.3. UAV PERFORMANCE UNDER DIFFERENT REYNOLDS NUMBERS..	48
4.4. FLOW BEHAVIOR INVESTIGATION FOR THE BEST CASE.....	49
CHAPTER V: CONCLUSION	51
REFERENCES	53



LIST OF TABLES

Table 1: Variables of V_1	19
Table 2: Variables of V_2	19
Table 3: Test Matrix	29
Table 4: Comparison of numerical results with the empirical correlation	39
Table 5: V_1 Parameters.....	42
Table 6: V_1 Parameters Analysis Results.....	44
Table 7: V_2 Parameters.....	46
Table 8: Flow Separation Estimation.....	52

LIST OF FIGURES

Figure 1: History of Aviation.....	1
Figure 2: Leonardo da Vinci's Sketches of Prone-Type Ornithopter and Helicopter	2
Figure 3: G. Cayley's Glider Sketches.....	3
Figure 4: O. Lilienthal in Flight.....	3
Figure 5: O. Lilienthal's Glider Design	4
Figure 6: Orville Wright's Flight with Flyer I.....	4
Figure 7: Newman [18] Experimental Schema.....	7
Figure 8: Coanda Patent "Perfectionnement aux Propulseurs"	9
Figure 9: H. Coanda's Original Patent	9
Figure 10: Coanda-1910 Jet	10
Figure 11: Robert Collins Aerial Flying Device Design.....	11
Figure 12: Geoffrey Hutton's First UAV Model.....	11
Figure 13: Geoffrey Hutton's Coanda Effect VTOL UAV	11
Figure 14: Jean Louis Naudin's GFS-UAV (N-01A).....	12
Figure 15: a) MEDIAS UAV Design [28] b) AESIR'S UAV Design	12
Figure 16: Schematic Detail of Benner's Test Section.....	13
Figure 17: Test Model for MAV of Schroyen and VanTooren	14
Figure 18: Velocity Magnitude Contour a) Circle Configuration b) Ellipse Configuration	15
Figure 19: Dimensions of The Designed UAV and Parametrical Presentation of The Optimized Parameters	18
Figure 20: Model Design and Excel Parameters.....	20
Figure 21: 3D Model View	20
Figure 22: V_1 Parameter (Radius of Curvature) a) $V_1= 110$ mm b) $V_1= 120$ mm....	21
Figure 23: V_2 Parameter (Arc Length) a) $V_2= 20$ mm b) $V_2= 25$ mm c) $V_2= 30$ mm	21
Figure 24: a) Pressure Force b) Viscous Force c) Resultant Force.....	26
Figure 25: Pressure and Shear Forces	26

Figure 26: The Longer Path Theory.....	28
Figure 27: Control volume representation of UAV Profile	31
Figure 28: Control Volume of Coanda Model	32
Figure 29: a) Fluent Area b) Model Geometry in Control Volume	34
Figure 30: Boundary Conditions.....	34
Figure 31: Mesh Domain.....	35
Figure 32: Inflation Geometries	36
Figure 33: Face Meshing Areas	36
Figure 34: Face Meshing Geometry Details	36
Figure 35: Mesh Independency Study.....	37
Figure 36: Validation study regarding to Bernoulli Equation.....	38
Figure 37: Turbulence model study	40
Figure 38: Parametrical View of the UAV	42
Figure 39: Rate of C_L/C_D Over Variable V_1 Values	43
Figure 40: Comparison of C_L/C_D Over h/R	43
Figure 41: Velocity Contours for a) $V_1=110$ mm b) $V_1=120$ mm c) $V_1=130$ mm ...	44
Figure 42: a) Early Separation b) Optimal Separation c) No Separation.....	45
Figure 43: Rate of C_L/C_D Over V_2	46
Figure 44: Velocity Contours Graphs a) $V_2=30$ mm b) $V_2=35$ mm c) $V_2=40$ mm ...	47
Figure 45: Velocity Performance According to C_L/C_D vs Radius	48
Figure 46: Velocity Magnitude Contour.....	49
Figure 47: Static Pressure Contour	49
Figure 48: Velocity Contour	50
Figure 49: Velocity Magnitude and Static Pressure Vectors	50
Figure 50: Turbulent Kinetic Energy Vector	50

LIST OF SYMBOLS AND ABBREVIATIONS

SYMBOLS

C_D	: Drag coefficient
C_L	: Lift coefficient
Cm	: Centimeter
D	: Drag force (N)
F_{CS}	: Force from Coanda surface (N)
F_{DP}	: Force from pressure difference between up and down parts (N)
h	: Height of duct
h_R	: Jet thickness on Coanda Surface (m)
l	: Length of cylindrical shape Coanda UAV (m)
L	: Lift force (N)
Lift _{Cylindrical}	: Total lift due to Coanda surface (N)
m	: Meter
\dot{m}	: Mass flow rate (kg/s)
mm	: Millimeter
p_a	: Atmospheric pressure (Pa)
p_s	: Surface pressure
p_∞	: Ambient pressure
R	: Radius of curvature
V	: UAV Velocity
V_{j-in}	: Jet inlet velocity

ABBREVIATIONS

CFD	: Computational Fluid Dynamics
UAV	: Unmanned Aerial Vehicle
VTOL	: Vertical Take-Off and Landing

CHAPTER I

INTRODUCTION

1.1. HISTORY OF AVIATION

The beginning and growth of aviation history have been made possible over the ages by people's curiosity about the sky. Many technologies that will mark a milestone in aviation history, from the first kite and hot air balloon flight to the first airplane and helicopter designs.

Since the beginning of 17-18th the century, people have made many attempts to develop the history of aviation. Self-lifting powered aircraft trials started in this period. The history of aviation has also developed with the development of methods that allow wings with sufficient lift and engines with sufficient thrust force to be developed. Although the first successful flight was in 1903, the first kite was flown in the fifth century BC, with balloons flying in the sky since 1783. The beginning and end of the first world war, the second world war and the second half of the twentieth century are the periods that played an important role in the history of world aviation [1].

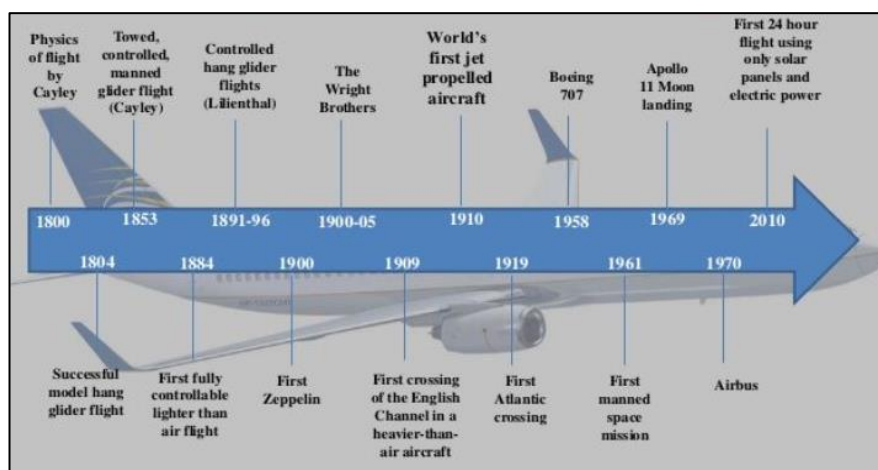


Figure 1: History of Aviation

The first kite was flown in China in the fifth century BC. From the 15th Century, kites could also be found in Europe. Active propellers first were used in hand-turned toys in Europe in the 14th Century. In fact, these are the rotor models that can be found from that period. Leonardo da Vinci drew models of ornithopters and helicopters from 1485 to 1490. He also produced the first sketches of the parachute and rotor.

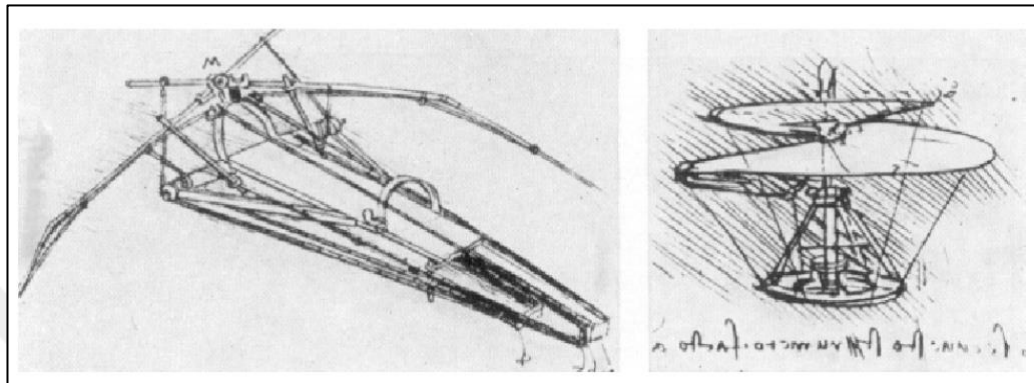


Figure 2: Leonardo da Vinci's Sketches of Prone-Type Ornithopter and Helicopter

George Cayley [2] is one of the pioneers of aviation. He discovered the basic principles of aerodynamics and studied weight, lift, drag and thrust forces that affect his performance in flight [3]. He discovered that in order to stabilize flight, the wings had to be fixed. As a result of his work, he introduced the basic concept of aircraft with separate systems for lift-thrust forces and control in 1799 [4-5]. Modern aircraft design is based on these foundations laid out by Cayley. He designed the first flying model airplane and continued to work on vertical flight. He designed the first reliable glider capable of carrying people. He studied four fundamental forces that affect flight performance. He argued that an engine that would provide thrust and lift should be developed to ensure continuous flight. He has been accepted as 'The Father of Aviation' with all these things [6-7].

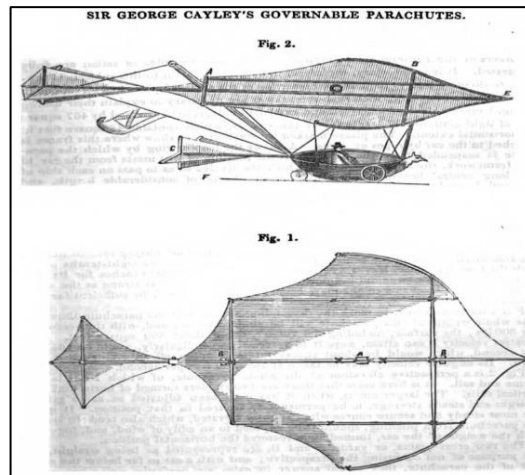


Figure 3: G. Cayley's Glider Sketches

Another of the 19th century's most important aviation pioneer was Otto Lilienthal. He was the first inventor to make successful flights with gliders. He conducted studies on aerodynamics and flight mechanics. He greatly contributed to the development of the modern wing concept [8-9]. He published his findings, which made important contributions to aviation, in the book "Der Vogelflug als Grundlage der Fliegekunst" (1889). His flight trials in 1891 were accepted as the beginning of human flight. The first aircraft in mass production was the "Lilienthal Normalsegelapparat", which he designed. Maschinenfabrik Otto Lilienthal thus became the first aircraft manufacturing company in the world [10].



Figure 4: O. Lilienthal in Flight

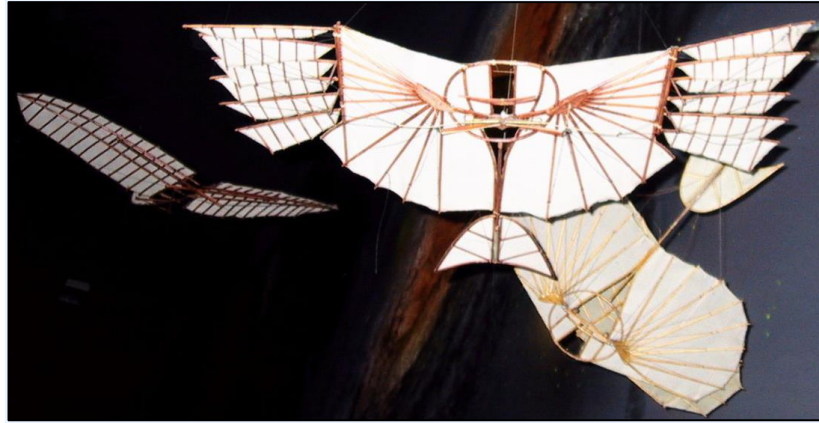


Figure 5: O. Lilienthal's Glider Design

The number of researches in the aviation industry has increased with public interest and technological progress. The American Wilbur and Orville Wright Brothers created the first airplane in the early 20th century, which helped launch modern aviation. The Wright Brothers tested their first airplane, the 'Flyer', in 1903. Flight trials were accepted as the first controlled and powered flights of heavier-than-air aircraft. In 1904-1905, the Wright Brothers developed the 'Wright Flyer II' and 'Wright Flyer III' designs and started to make longer flights. The Wright Flyer III is recognized as the first truly practical fixed-wing aircraft model with more aerodynamic flight. They continued their work on designing a three-axis control system that allows the pilot to steer the aircraft effectively and balanced [11-12]. With this control system approach, the Wright brothers made efficient blade and propeller designs. They got their patents on aerodynamic control systems [13]. With their work, they became experts in aerodynamics and piloting.

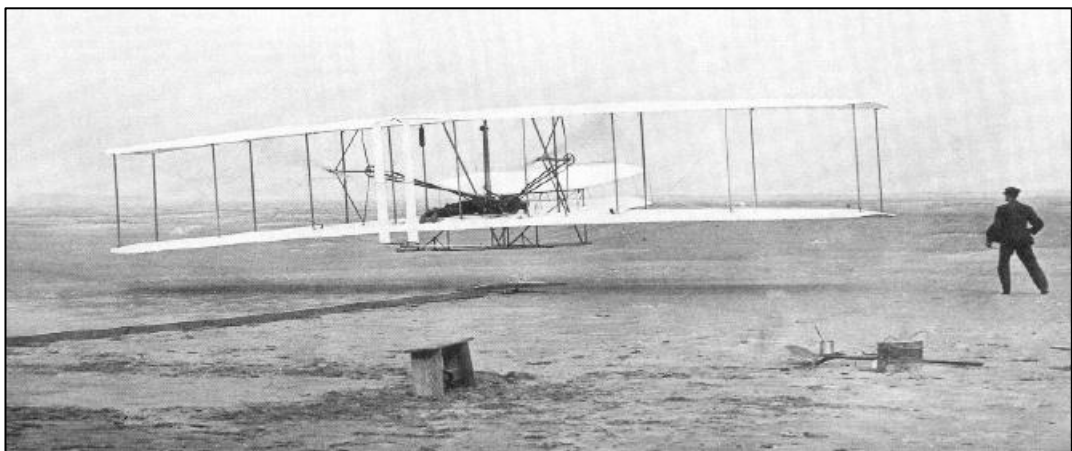


Figure 6: Orville Wright's Flight with Flyer I

Following these innovations, French engineer Paul Cornu flew the first powered helicopter. Demands in all facets of aviation have begun to rise due to the development of all these aircraft and technologies. Numerous vehicles have been developed and constructed for usage in industries like civil aviation, the military, and transportation. Only those of these tools that are still capable of being created and improved are still in use today. In this context, Unmanned Aerial Vehicles (UAVs), aviation branch, are frequently used.

1.2. UNMANNED AERIAL VEHICLE

Unmanned aerial vehicles (UAVs) are aircraft designed to communicate with the controller on the ground without a pilot. Remote controls and GPS systems can be used to operate UAVs. These vehicles can be employed for civil, commercial, military, and recreational purposes. After the First World War, Archibald Montgomery Low created the first unmanned aerial vehicle (UAV). UAV designs were created and modernized throughout World War II and the following wars.

UAVs have recently assumed important roles in several industries thanks to their cost and mobility. It can be relocated to the intended location easily because there isn't a physical pilot. Due to their ability to hover, take off vertically, and carry payloads, UAVs have a variety of applications. Usage areas nowadays have significantly expanded based on a wing and engine type, fuel system, and take-off-landing type.

1.3. COANDA EFFECT

The Coanda effect is the name given to the phenomenon where a fluid moving at a certain speed moves forward by clinging to the surface slope instead of following a straight path. The fluid jet approaching the curved surface tends to remain attached to the surface. An example of this effect is that the liquid pouring from the glass follows the inclination of the glass or the water flowing from the tap follows the surface of the spoon brought in front of it.

This phenomenon was explained by Thomas Young at a lecture given in 1800: *“The lateral pressure which urges the flame of a candle towards the stream of air from a blowpipe is probably exactly similar to that pressure which eases the inflection of a current of air near an obstacle. Mark the dimple which a slender stream of air makes on the surface of water. Bring a convex body into contact with the side of the stream and the place of the dimple will immediately show the current is deflected towards the body; and if the body be at liberty to move in every direction it will be urged towards the current...”* (Young 1800: 14).

In the early 1900s, Henri Coandă discovered an application of this effect as a result of an experiment with an airplane. Henry Coanda noticed that the air pushed back by the engine-powered turbine was drawn to the surface near it. After this event, he made various studies and received patents. The Coanda effect is observed when the propeller creates a flow parallel to the surface on the airfoil. The flow around the airfoil creates a pressure difference. Thus, a swirl perpendicular to the direction of movement is formed in the wings and the bearing force is obtained [15]. Due to the Coanda effect used in aerodynamics, convex curved surfaces tend to pull the fluid above them into the region of lower pressure [16-,17]. The Coanda effect can be used to create an increase in two situations:

- To change the direction of the upward thrust airflow to point downwards.
- To drag the air causing lift by creating a low-pressure zone on the surface.

Scientific studies on the Coanda effect have been going on for years. In his research, Newman [18] described an incompressible, two-dimensional turbulent jet flowing over a circular cylinder surface. According to this study, the Coanda adhesion effect is directly related to the forces applied to the fluid. Two important forces that keep it on a curved surface are centrifugal force and radial pressure [18-19]. As the jet exits the curvature, the contact pressure is lower than the ambient pressure due to the viscous drag created by the interaction of the fluid and the curved surface.

The fundamental reason why a fluid jet sticks to a curved wall surface is because of this pressure difference.

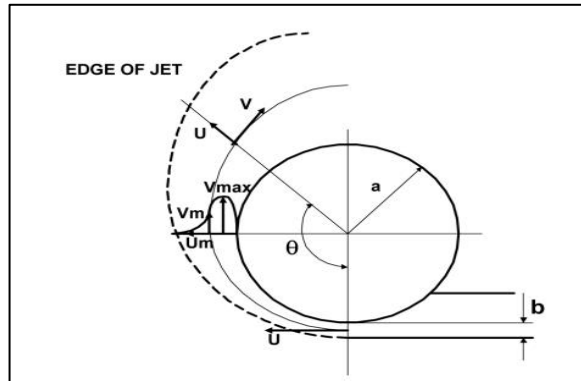


Figure 7: Newman [18] Experimental Schema

The Coanda Effect was described in terms of an inviscid irrotational flow by Bradshaw [20]. The formula that explains the pressure behavior of the flow is obtained from the Bernoulli equation under the assumption that the flow is initially inviscid:

$$p_0 = p_\infty - \frac{\rho U^2 b}{a} \quad (1.1)$$

There is ρ : Density of the jet fluid, U : Mean velocity, b : Slot width, a : Radius of wall

The pressure of the inviscous fluid is lower than the ambient pressure until:

$$\frac{\rho U^2 b}{a} \leq p_\infty \quad (1.2)$$

The expression in the above equations is suitable for making a general definition. The engagement between the fluid jet and the curved surface produces a reduction in average velocity due to the reverse pressure gradient. Accordingly, it is expected that the thickness of the jet advancing on the surface will increase. In such viscous flows, as the surface pressure increases along the wall, the average velocity decreases and becomes equal to the ambient pressure. Theoretically, when $P_s = P_\infty$, the flow leaves the curved surface [20]. The main cause of jet separation from the curved wall is viscous effects.

1.4. COANDA EFFECT VTOL UAV

Most unmanned aerial vehicles (UAVs) have fixed wings like regular airplanes. However, these models cannot hover, have limited payload and maneuverability, and need a runway to take off and land since the plane's wings only lift while moving through the air. These issues are overcome by Vertical Take Off and Landing (VTOL) UAVs, which typically use rotors similar to a helicopter. This is significant because a UAV's ability to do the vertical take-off and landing (VTOL) is highly necessary [21].

Nevertheless, because they must employ several rotors to fly, they have some drawbacks regarding flight time, safety, etc. Thus, there have been numerous attempts to design UAVs with just one rotor.

A new class of VTOL vehicles UAVs that utilize the Coandă Effect have emerged over the last ten years. To create lift and achieve stability in their function as a surveillance platform, VTOL UAVs use the Coandă effect. The lift forces of UAVs are generated by diverting and streamlining the air flow over the upper curved surface that is outside the propeller. The upper propeller produces an airstream that is adherent to a curved surface. The curved surface is the area where the Coanda effect is effective. The Coandă effect causes the air above the upper surface to move more quickly, which decreases the air pressure near it and increases lift in this area, producing the necessary lift forces. The Coandă UAV balances its weight in this manner and hovers in the direction of the lift forces produced on the upper surface of the fuselage. UAV creates lift force in this way, enabling vertical take-off and landing.

Since Henri Coanda's first patent application for a propulsion system utilizing the "Coanda effect" was made in 1938 [22], numerous modifications of this system have been tried by researchers worldwide [23].

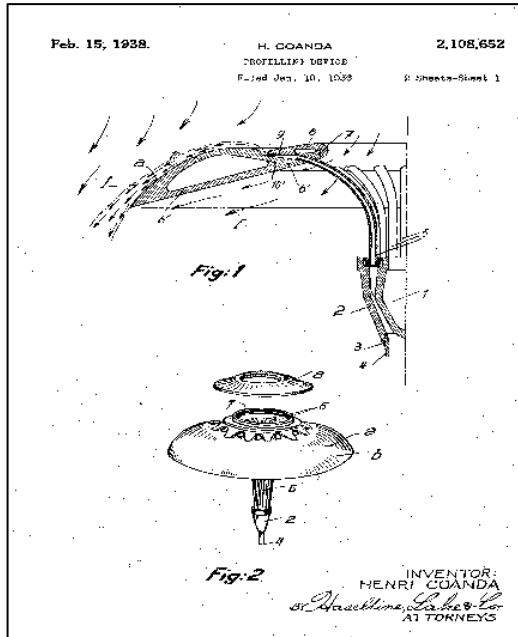


Figure 8: Coanda Patent "Perfectionnement aux Propulseurs"

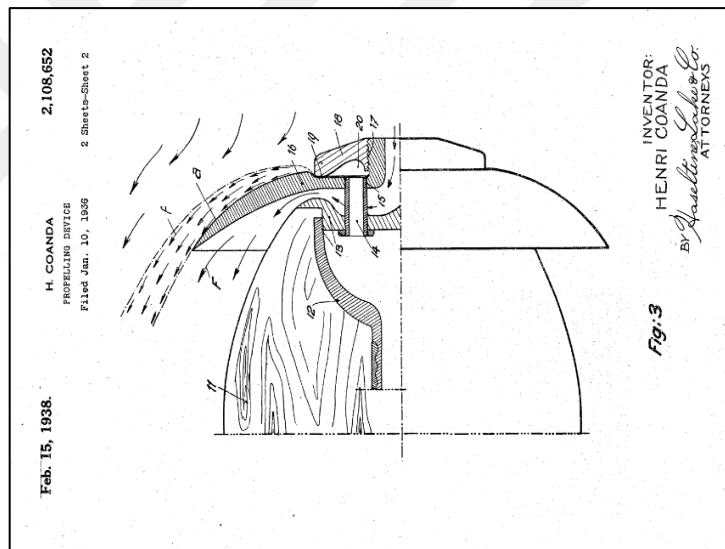


Figure 9: H. Coanda's Original Patent

1.4.1. Coanda UAV Background

Henri Coanda designed and built the world's first airplane with a jet reactive propulsion system in early 1910. This aircraft, known as the Coandă -1910 Aircraft, was also the first to apply the Coandă effect [22].

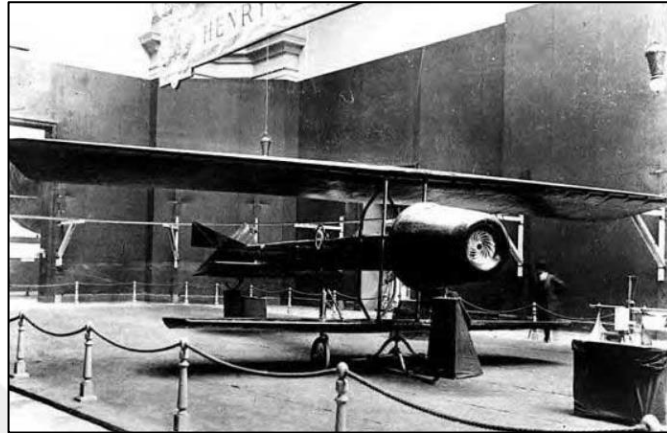


Figure 10: Coanda-1910 Jet

Following the year 2000, the Coandă effect was primarily used in the development of a new class of aircraft by certain aviation inventors, including Geoffrey Hatton (2002), Collins (2002) and Naudin (2006).

In one of his innovations in the UK, Robert Collins valued the Coanda Effect capabilities which was awarded GB patent number 2387158 in 2003. In his article "Coanda - A New Airspace Platform for UAVs," presented at the Bristol International UAV Conference in April 2002 [24-25], this new Coandă application was already described. The air is drawn in from above the craft and blown out radially. Over the top of the curving body, by the rotor at the center of the hollow fuselage canopy. The airstream follows the curved surface of the canopy due to the Coandă Effect, leaving the body at the base.

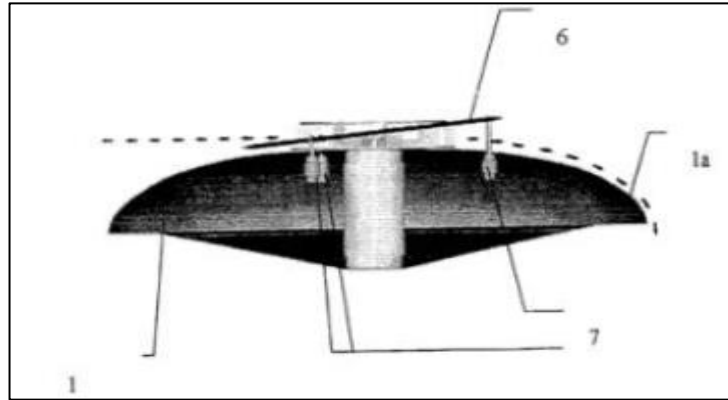


Figure 11: Robert Collins Aerial Flying Device Design

Geoffrey Hutton, a British inventor, and the GFS (Geoff's Flying Saucers) project team proposed a Coandă Effect UAV with a circular canopy in the 1990s. The circular design changed when GFS projects created their first model, becoming octagonal with flat flaps on four opposing sides of the trailing edge [26].

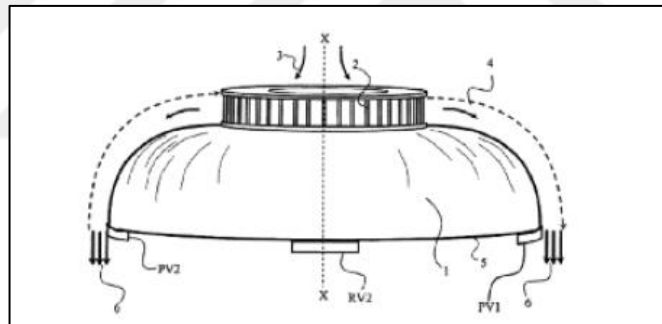


Figure 12: Geoffrey Hutton's First UAV Model



Figure 13: Geoffrey Hutton's Coanda Effect VTOL UAV

Jean Louis Naudin [27] made his unmanned aerial vehicle in 2006 by reviewing the GFS project's concept. It has created a vehicle with characteristics comparable to the helicopter, which can take off vertically and take off and hover by utilizing the Coanda effect, by using electric motors in its model. Geoff Hatton's vehicle from GFS Project Limited inspired J.L. Naudin's design of the UAV N-01A.

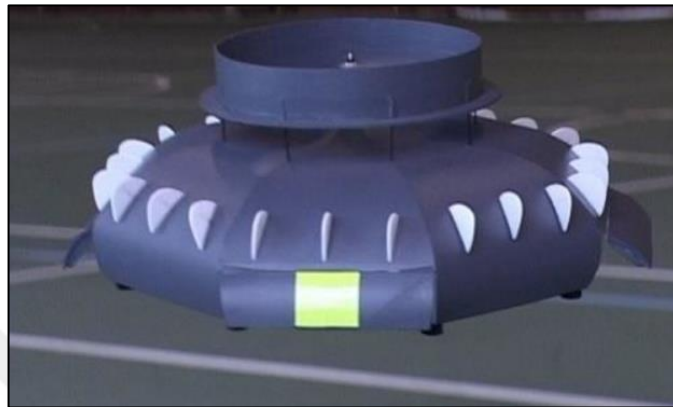


Figure 14: Jean Louis Naudin's GFS-UAV (N-01A)

GFS Projects LTD (a French company), AESIR Ltd (a British company), MEDIAS project and others developed aerial vehicles that use the Coandă effect.



Figure 15: a) MEDIAS UAV Design [28] b) AESIR'S UAV Design

Mirkov and Rasuo [31] performed Coanda effective simulation modeling in 2010 and 2012. With the Coanda jet effect, they noticed that the wall jet followed the surface of the curvature for a while before leaving. This causes a reduction in the diameter of a swirl ring. Thus, a pressure force is created which causes the surrounding air to be entrained and pushed upwards from the lower part of the surface. At the end of all this research, they observed that geometry had a significant impact on the process. They stated that there are models similar to elliptical-springs used in these vehicles in general.

Schroijen and VanTooren [32] simulated the cylindrical Coanda effect configuration, which reduced vehicle aerodynamic losses and significantly eliminated drag compared to previous studies. At the scale of a micro-aerial vehicle (MAV) as shown in Figure 17, with no moving parts and a centrifuge wrapped around the flow generator, this model examines the 'lift-to-weight ratio' parameter. In their study, they observed the effects of design parameters on performance. They studied different models of radius of curvature and compared them. They observed that working on an elliptical model rather than a circular curve and decreasing the radius of curvature after certain ratio increases thrust as shown in Figure 18.

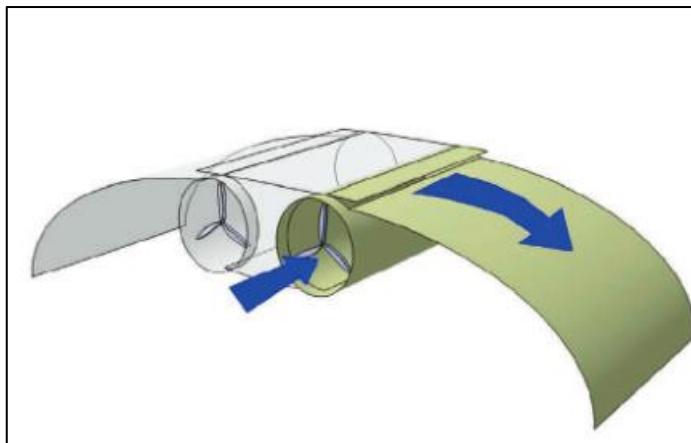


Figure 17: Test Model for MAV of Schroijen and VanTooren

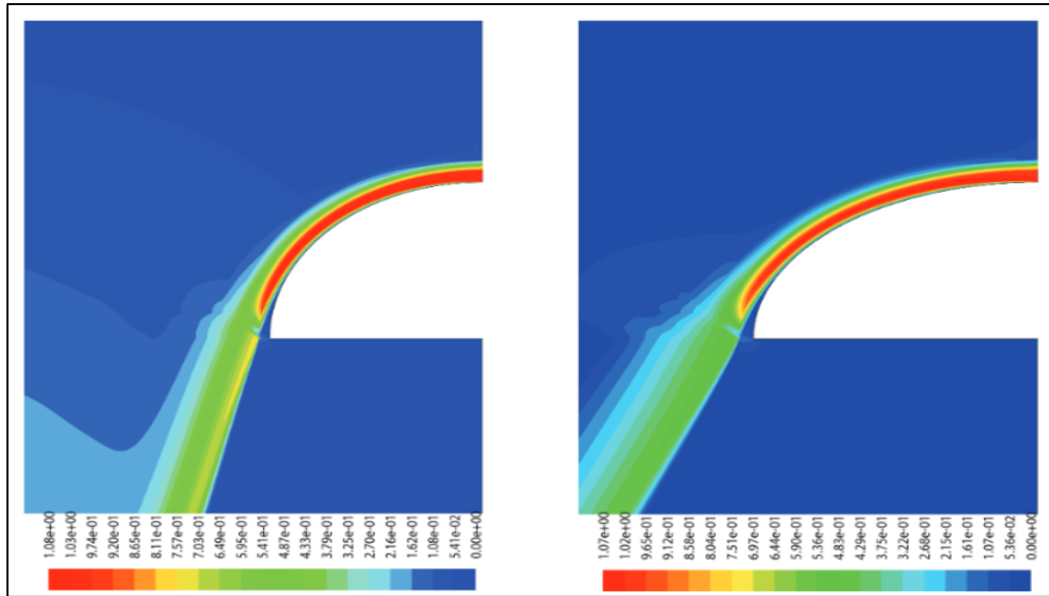


Figure 18: Velocity Magnitude Contour a) Circle Configuration b) Ellipse Configuration

Dragan [33], Wessapakdee et al. [34], and Florescu et al. [35] have also conducted similar studies on the Coanda effect on saucer models, and their findings will be addressed for their associated viewpoints.

1.5. AIM OF THESIS

Unmanned Aerial Vehicles (UAV) are air vehicles that play a role in every field today. The majority of UAVs are built with propulsion that follows one of the two main systems in order to complete their special duties. First, some models have fixed wings that resemble a conventional airplane. They need a runway for takeoff and landing. Others are models that can take off and land vertically (VTOL) and use their rotors like a helicopter. Vertical take-off and landing (VTOL) capabilities are desired features of aircraft, provided high flight performance is offered. Today, UAV designs are beginning to incorporate functionality of taking off. UAVs don't need a long runway or a big space to take off and land vertically.

UAVs have some drawbacks due to employing more than one rotor for flight, notwithstanding the benefits of vertical takeoff and landing. Scientists have therefore begun to develop airplanes that just require one rotor to operate. The Coanda effect enables the development of vehicles with a single engine that can fly [24]. The Coanda Effect UAVs have been developed to produce lift and maneuverability more efficiently. It moves more quickly than a helicopter yet can take off and land just like one. Thanks to this effect, the air entering from the propeller is pulled directly onto the vehicle's surface. The viscosity of the fluid moving along the surface creates friction between the fluid and the surface. According to Newton's third law, the flow is drawn towards the surface. Flow pulled onto the surface tends to flow across unless the surface curvature is very sharp. Thus, the flow flowing from the surface creates a low-pressure area where it passes. The buoyancy force, which Navier-Stokes equation can explain, is thus generated. In this way, it creates a lifting force for single rotor VTOL vehicles. However, since the Coanda effect is an unstable flow affected by some complex factors, its formulation and analysis cannot be done precisely. When the studies were examined, it was decided that the most suitable method for analyzing this subject was the investigation of an oval-shaped surface. The main issue for the VTOL UAV that will work with the Coanda effect is examining the surface modeling that creates maximum lift and minimum friction forces. In this thesis, the numerical effects of the parameters created to provide the Coanda effect on the prepared model will be examined. Surface optimization that provides maximum lift and minimum drag force is performed with using the Computational Fluid Dynamics Tools (CFD). The separation angle that provides the optimum values will be determined.

CHAPTER II

MECHANICAL DESIGN

In this study, first of all, concept design research is conducted. Parameters that have a direct effect on the performance have been determined according to the working principle of the Coanda effect. These parameters have been optimized to create maximum lift and minimum drag forces. The center of gravity and the center of symmetry of the designed model should be in the vertical direction. As indicated in Figure 19, there is a propeller duct on the top of the model that will blow the air down directly without dispersing it. The air coming from the propeller is separated from the curved surface by the flaps at the bottom of the model. The lift force is obtained by the swirl that occurs during this separation process.

Autodesk Inventor and SolidWorks softwares were used to design three-dimensional shapes according to the parameters determined while designing the surface. In the Figure 19, the blower, duct and surface form the basic structure of the model is depicted. The first parameter under investigation is the radius of the model (V_1) that is important because the air blown from the blower will stick to the surface and create a Coanda effect. The other parameter that has a direct effect on the lift is the arc length (V_2) that is related to the flap surfaces and an effective parameter in changing the flow direction. The limits of V_1 and V_2 parameters are indicated in Table 1-2.

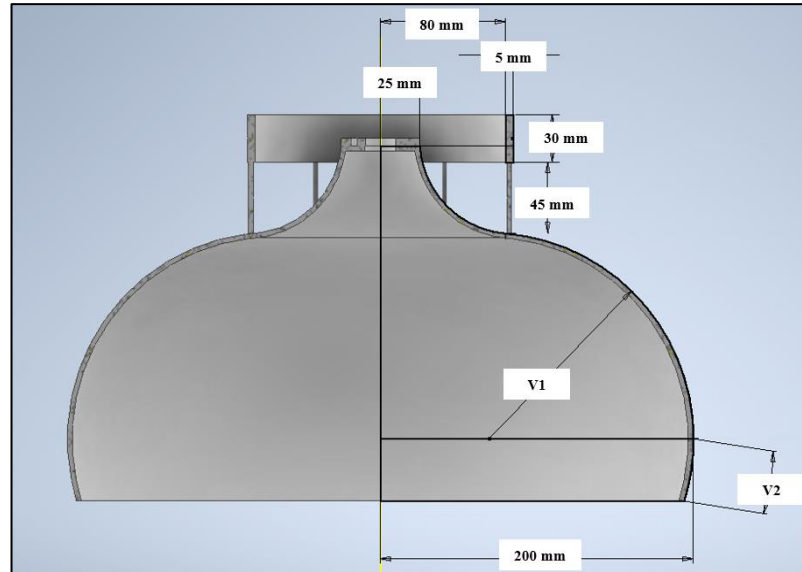


Figure 19: Dimensions of The Designed UAV and Parametrical Presentation of The Optimized Parameters

The lift force to be obtained from the Coanda surface is directly dependent on the radius of curvature (V_1 Parameters). In this context, it is expected that maximum velocity and minimum pressure areas will occur when creating analyzes on the surface.

The flow downstream from the Coanda surface must separate after passing the critical radius of curvature. In this way, since the flow will not accelerate on the flap surfaces, it will not be difficult for the model to balance in the air. Arc length variables (V_2 Parameters) are the parameters that will be observed to separate the flow from the flap surface. The radius of the model is determined as 200 mm. The propeller radius was kept constant at 80 mm and the distance between the channel and the surface was 45 mm.

Limits are specified for parameters V_1 and V_2

Table 1: Variables of V_1

Parameter	Variables
V_1 (Radius of Curvature Parameters)	110 mm
	120 mm
	125 mm
	130 mm
	135 mm
	140 mm

Table 2: Variables of V_2

Parameter	Variables
V_2 (Arc Length Parameters)	20 mm
	25 mm
	30 mm
	40 mm
	45 mm

V_1 and V_2 design parameters were created in excel and adapted to the Autodesk Inventor program. Thus, the models were created with a parametric design. as shown in Figure 20. In Figure 21, three-dimensional model of the UAV is depicted.

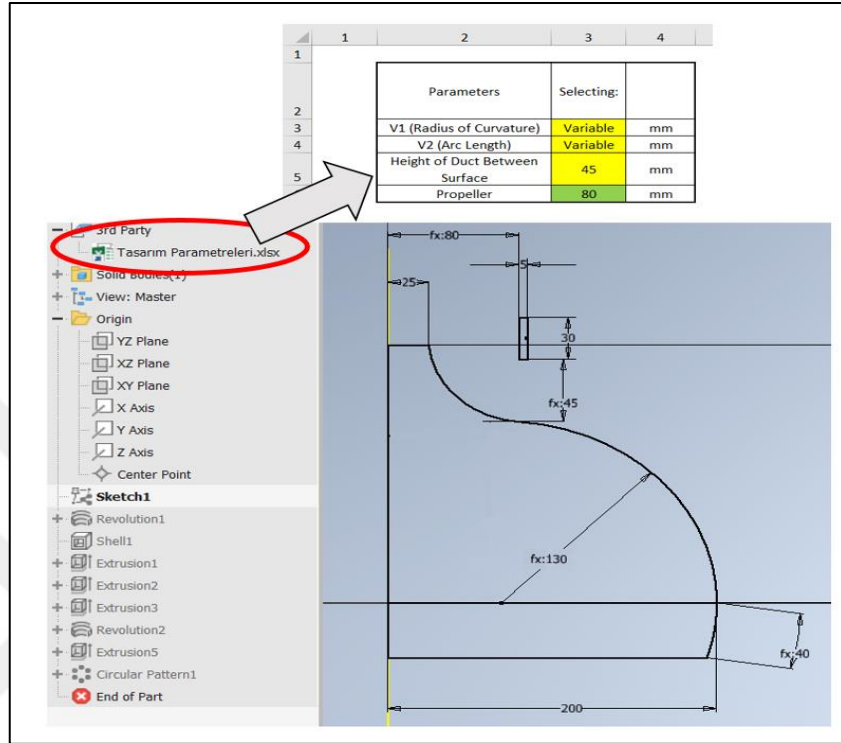


Figure 20: Model Design and Excel Parameters

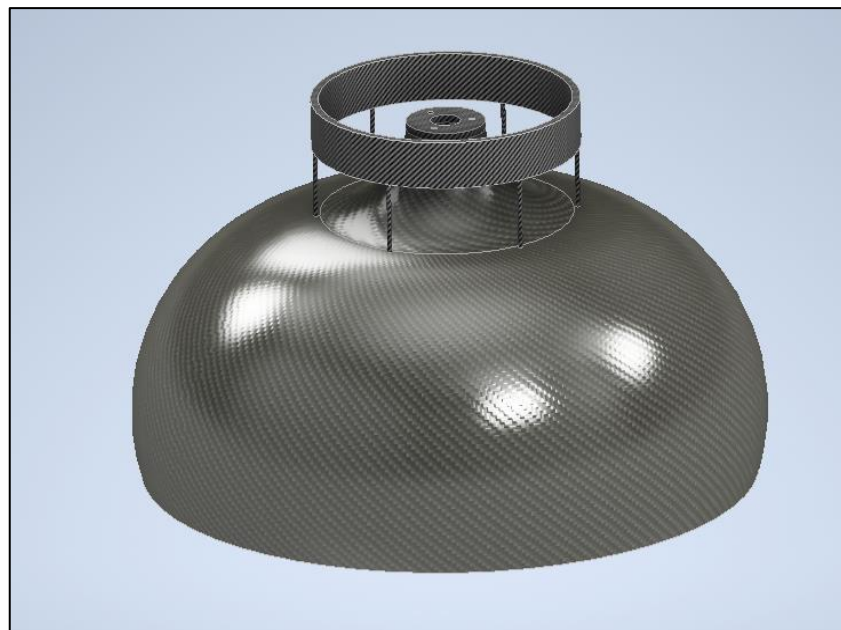


Figure 21: 3D Model View

Comparisons of the radius of curvature and arc length variables constrained as parameters V_1 and V_2 are shown in the Figure 22 and Figure 23.

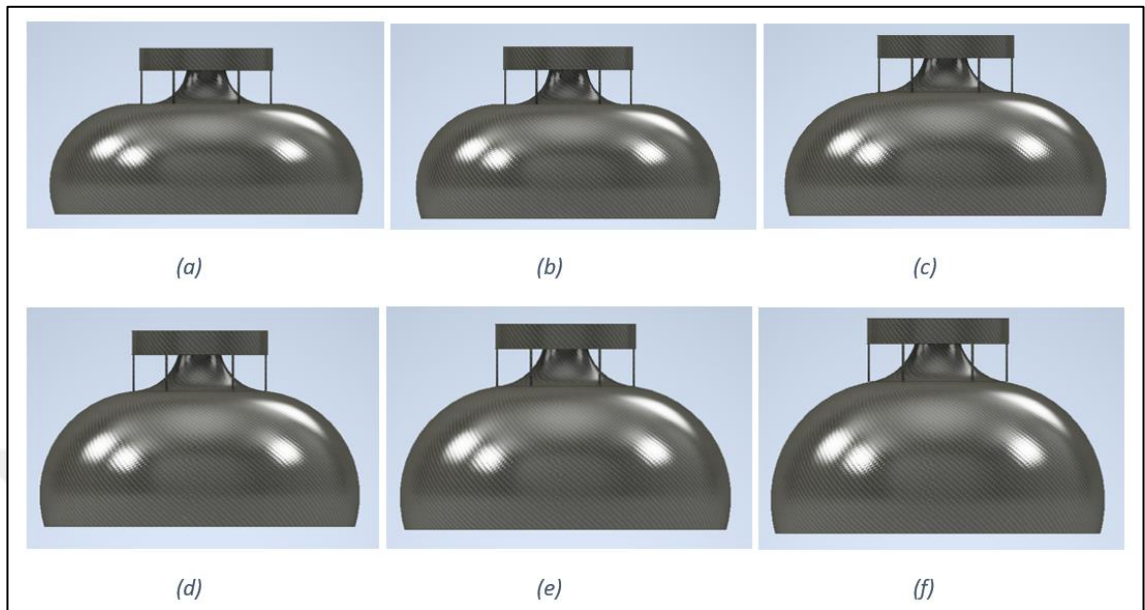


Figure 22: V_1 Parameter (Radius of Curvature) a) $V_1= 110$ mm b) $V_1= 120$ mm
c) $V_1= 125$ mm d) $V_1= 130$ mm e) $V_1= 135$ mm f) $V_1= 140$ mm

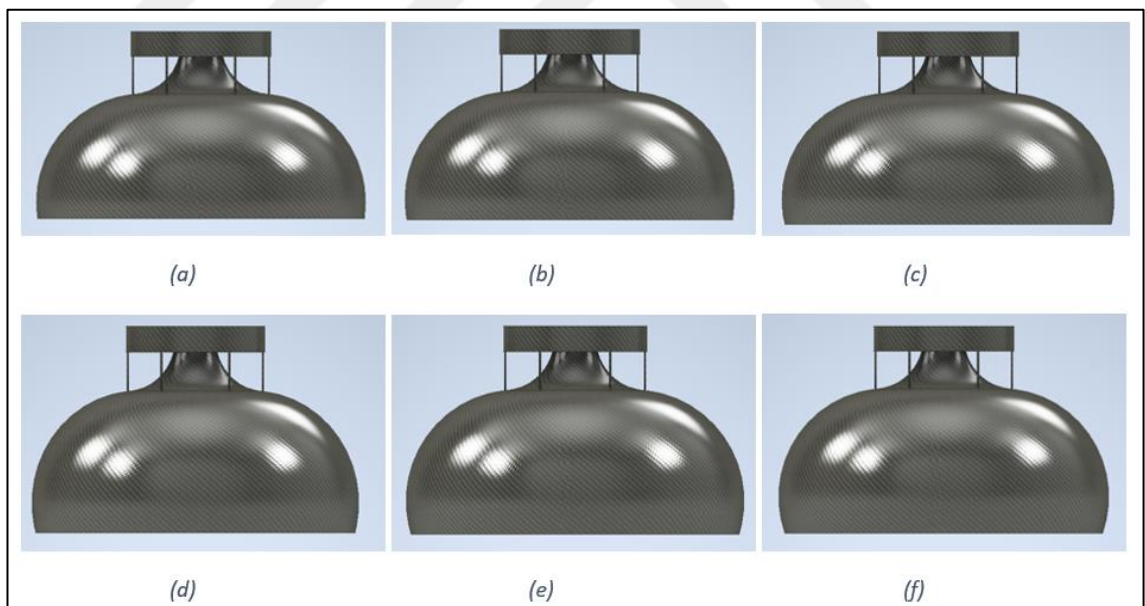


Figure 23: V_2 Parameter (Arc Length) a) $V_2= 20$ mm b) $V_2= 25$ mm c) $V_2= 30$ mm
d) $V_2= 35$ mm e) $V_2= 40$ mm f) $V_2= 45$ mm

CHAPTER III

NUMERICAL METHODOLOGY

Coanda Effect UAV model analyses performed with the help of CFD methods. All simulations are assumed to be turbulent, three dimensional, incompressible and inviscid. Computational Fluid Dynamics simulations are performed using the ANSYS Fluent program, which solves the incompressible Navier-Stokes equations using the cell-based least squares method for calculating gradients and derivatives.

3.1. PHYSICAL AND MATHEMATICAL EXPRESSION OF TURBULENCE

3.1.1. Physical Expression of turbulence

The physical expression of turbulence is expressed by the ratio of the inertial force of the fluid to the viscous force and the Reynolds number, which is a dimensionless number. The Re number depends on the density (ρ), velocity (U), viscosity (μ) of the fluid, and the characteristic length of the body with which the fluid contacts, and is expressed as given in the equation below.

$$Re = \frac{\rho U D}{\mu} = \frac{\text{Inertial Forces}}{\text{Viscous Forces}} \quad (3.1)$$

3.1.2. Mathematical Expression of Turbulence

To solve compressible flow motion, it is necessary to solve the mass, momentum and energy equations. These equations are expressed as given below.

$$\frac{\partial \rho}{\partial t} + \frac{\partial(\rho u_i)}{\partial x_i} = 0 \quad (3.2)$$

$$\frac{D(u_i)}{Dt} = \frac{\partial u_i}{\partial t} + u_j \frac{\partial u_i}{\partial x_j} = -\frac{1}{\rho} \frac{\partial P}{\partial x_i} + \nu \frac{\partial^2 u_i}{\partial x_j^2} + F_i \quad (3.3)$$

$$\frac{\partial}{\partial t} \left[\rho \left(e + \frac{1}{2} u_i u_i \right) \right] + \frac{\partial}{\partial x_j} \left[\rho u_j \left(h + \frac{1}{2} u_i u_i \right) \right] = -\frac{\partial}{\partial x_j} (u_i t_{ij}) + \frac{\partial q_j}{\partial x_j} \quad (3.4)$$

In Equation 3.4, e denotes internal energy, h , and specific enthalpy. For compressible flows, the term t_{ij} is the viscous stress tensor containing the term ζ secondary viscosity and μ the molecular viscosity term. This term is defined as:

$$t_{ij} = 2\mu S_{ij} + \zeta \frac{\partial u_k}{\partial x_k} \delta_{ij} \quad (3.5)$$

In the equation, S_{ij} is the angular deformation term and δ_{ij} is the Kronecker delta term. The term ζ secondary viscosity can be written as $\zeta = -\frac{2}{3}\mu$. Solving the continuity, momentum and energy together, the unknown velocity, pressure, temperature, and density values are calculated. Since the Navier-Stokes equations do not have an analytical solution, these equations are solved by CFD programs with the help of numerical methods.

3.1.3. Modeling of Turbulence and Numerical Approaches

The most important difference between turbulent and laminar flow is that the flow parameters exhibit random and irregular behavior in turbulence. These irregularities occur in the x , y and z velocity components, pressure gradients, shear stress, temperature, and all other parameters that determine the flow field. The oscillations to which these data are exposed can be of small scale and high frequency. At high Reynolds numbers, it is impossible to solve the Navier-Stokes equations for all scales; In this context, the Reynolds mean approach is used. The oscillations in the parameters in the Navier-Stokes equations are separated into the mean and the oscillating part. For instance, Equation 3.6 provides a decomposition of the turbulent velocity parameter.

$$u_i = \tilde{u}_i + u_i'' \quad (3.6)$$

When each term in the conservation equations is changed to be group-mean (Reynolds Mean) or ignoring small scales, as indicated in equation 3.6, equations 3.7, 3.8, and 3.9 are obtained. As seen from the equations, the RANS technique adds new unknowns into the conservation equations, and only turbulence models may be used to simulate these unknown parameters.

$$\frac{\partial(\bar{\rho}\tilde{u}_i)}{\partial x_i} = 0 \quad (3.7)$$

$$\frac{\partial\bar{\rho}\tilde{u}_i}{\partial t} + \frac{\partial(\bar{\rho}\tilde{u}_i\tilde{u}_j)}{\partial x_i} = -\frac{\partial P}{\partial x_i} + \frac{\partial}{\partial x_j} \left[\bar{t}_{ij} - \overline{\rho u_j'' u_i''}^* \right] \quad (3.8)$$

$$\begin{aligned} & \overbrace{\frac{\partial}{\partial t} \left[\bar{\rho} \left(\tilde{e} + \frac{\tilde{u}_i \tilde{u}_i}{2} + \frac{\bar{\rho} u_i'' u_i''}{2} \right) \right]}^A + \overbrace{\frac{\partial}{\partial x_j} \left[\bar{\rho} \tilde{u}_j \left(\tilde{h} + \frac{\tilde{u}_i \tilde{u}_i}{2} + \tilde{u}_j \frac{\bar{\rho} u_i'' u_i''}{2} \right) \right]}^B = \\ & \overbrace{\frac{\partial}{\partial x_j} \left[-q_{ij} - \bar{\rho} u_j'' h'' + \bar{t}_{ij} \bar{u}_i'' - \bar{\rho} u_j'' \frac{1}{2} u_i'' u_i'' \right]}^C + \overbrace{\frac{\partial}{\partial x_j} \left[\tilde{u}_i (\bar{t}_{ij} - \bar{\rho} u_j'' u_i'') \right]}^C \end{aligned} \quad (3.9)$$

In these equations, $\bar{\rho}$ is the mean density, \tilde{u}_i is the mean velocity, P is the mean pressure, \bar{t}_{ij} is the total stresses, \tilde{e} is the unit mass and \tilde{h} is the mean energy. Equation 3.9 is the energy equation, consisting of internal energy, average flow kinetic energy, and turbulent kinetic energy. At these three energies, it adds additional unknown terms representing physical properties to the total energy equation.

'A' and 'B' are terms of kinetic energy due to turbulent oscillations. The terms $\bar{t}_{ij} \bar{u}_i''$ and $\frac{\bar{\rho} u_j''}{2 u_i'' u_i''}$ in 'C' and 'D' represent molecular diffusion and turbulent transport of turbulent kinetic energy. In Equation 3.8, the term (*) is the Reynolds stress term.

This term expresses the convection of mean momentum due to turbulence and is the term that distinguishes turbulent flow from laminar flow. This equation cannot be solved analytically. Turbulence models provide approaches for modeling this equation. Reynolds stress in compressible flows in zero, one and two-equation models are often solved using the Boussinesq approach, and the relation of Reynolds stresses to velocity gradients according to the Boussinesq hypothesis is as follows:

$$\rho \tau_{ij} = \bar{\rho} \tilde{u}_j \tilde{u}_i'' = 2\mu_t \left(S_{ij} - \frac{1}{3} \frac{\partial u_k}{\partial x_k} \delta_{ij} \right) - \frac{2}{3} \bar{\rho} k \delta_{ij} \quad (3.10)$$

Turbulence models are used in this approach to solve the turbulent viscosity term (t).

3.1.4. The SST k- ω Turbulence Model

The SST k- ω turbulence model [Menter 1993] is a two-equation eddy viscosity model. The k- ω based SST turbulence model calculates turbulent shear stresses and predicts the onset of flow separations and the amount of shear under reverse pressure gradients [36].

Using the k-w formulation on the inside of the boundary layer makes it usable directly from the viscous substrate to the wall so the SST k- ω turbulence model is used with the Reynolds-averaged Navier–Stokes equations approach.

$$\mu_t = \rho \frac{k}{\omega} \quad (3.11)$$

The k-w model solves two transfer equations, the first is turbulent kinetic energy, k, and the second is turbulent frequency, ω . The stress tensor is calculated according to the eddy-viscosity concept. Respectively, the k equation (3.12) and the ω equation are explained in (3.13).

$$\frac{\partial(\rho k)}{\partial t} + \nabla \cdot (\rho U k) = \nabla \cdot \left[\left(\mu + \frac{\mu_t}{\sigma_k} \right) \nabla k \right] + P_k - \beta' \rho k \omega \quad (3.12)$$

$$\frac{\partial(\rho \omega)}{\partial t} + \nabla \cdot (\rho U \omega) = \nabla \cdot \left[\left(\mu + \frac{\mu_t}{\sigma_w} \right) \nabla \omega \right] + \alpha \frac{w}{k} P_k - \beta \rho \omega^2 \quad (3.13)$$

' P_k ' is the amount of turbulence production.

$$P_k = \mu_t \nabla U \cdot (\nabla U + \nabla U^T) - \frac{2}{3} \nabla \cdot U (3\mu_t \nabla \cdot U + \rho k) + P_{kb} \quad (3.14)$$

The model constants are given below.

$$\beta' = 0.09$$

$$\alpha = \frac{5}{9}$$

$$\beta = 0.075$$

$$\sigma_k = 2$$

$$\sigma_w = 2$$

3.2. AERODYNAMICS PERFORMANCE INVESTIGATIONS

Interactions occur between an object moving in the fluid and the fluid. These interactions are the forces between the fluid and the body. These forces can be: wall shear stresses (τ_w), normal stresses due to pressure and stresses due to viscous effects.

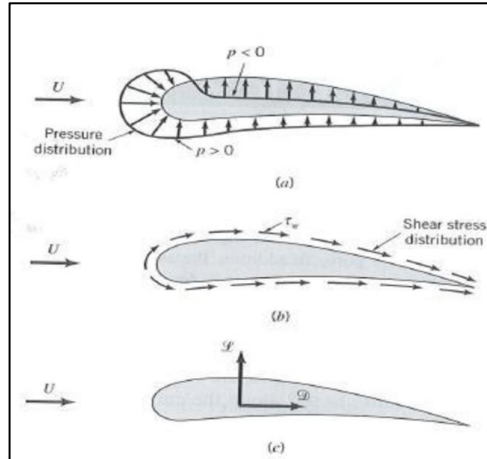


Figure 24: a) Pressure Force b) Viscous Force c) Resultant Force

In Figure 25, the force acting in the upstream direction is called drag (\mathcal{D}), and the resultant force normal to the upstream velocity is called lift (\mathcal{L}).

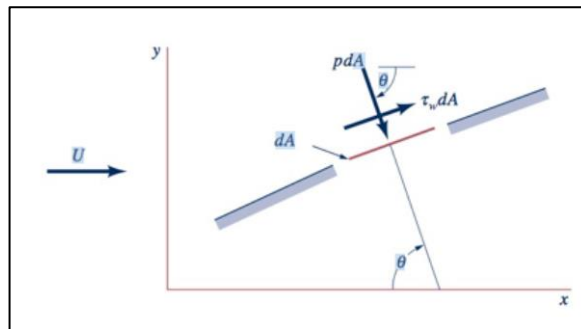


Figure 25: Pressure and Shear Forces

By integrating the effect of these two variables on the body surface, the resultant shear stress and pressure distributions may be calculated.

The fluid force on the small area element dA has the following x and y components:

$$dF_x = (p \, dA) \cos \theta + (\tau_w \, dA) \sin \theta \quad (3.16)$$

$$dF_y = -(p \, dA) \sin \theta + (\tau_w \, dA) \cos \theta \quad (3.17)$$

$$D = \int dF_x = \int p \cos \theta \, dA + \int \tau_w \sin \theta \, dA \quad (3.18)$$

$$L = \int dF_y = -\int p \sin \theta \, dA + \int \tau_w \cos \theta \, dA \quad (3.19)$$

Eqs. 3.18. and 3.19. cannot be applied without comprehensive knowledge of a body's shear stress and pressure distributions. The more common approach is to create dimensionless lift and drag coefficients and estimate their values using a simplified analysis, a numerical method, or a suitable experiment. The lift coefficient, C_L , and drag coefficient, C_D , are explained as follows:

$$C_L = \frac{L}{\frac{1}{2}\rho U^2 A} \quad (3.20)$$

$$C_D = \frac{D}{\frac{1}{2}\rho U^2 A} \quad (3.21)$$

where A is a characteristic area of the object: the area viewed from the direction parallel to the flow velocity, the area normal to the velocity upstream towards the object.

Lift and drag are two important terms for understanding the fundamentals of aerodynamics. Lift is the aerodynamic force that keeps an airplane airborne while moving and balances the gravitational force. One can infer that fluid velocity across a wing's surface is the source of the lift and the other aerodynamic forces. This way, it coexists with drag, another significant aerodynamic force that is influenced by the aircraft's velocity. Drag is almost always used to describe how something is impeding forward progress. Also drag significantly impacts aerospace vehicles' propensity to stay on course.

According to the "Longer Path" theory, air molecules passing over the top of an aerofoil have a longer distance to go than those passing underneath because aerofoils are formed with the upper surface being longer than the bottom. According to the theory, the air molecules must all arrive at the trailing edge at the same time, and for that to happen, the molecules crossing the top of the wing must move more quickly than those crossing the underside.

According to Bernoulli's equation, the faster, higher flow results in lower pressure, which causes the difference in pressure across the airfoil so lift is producing [37].

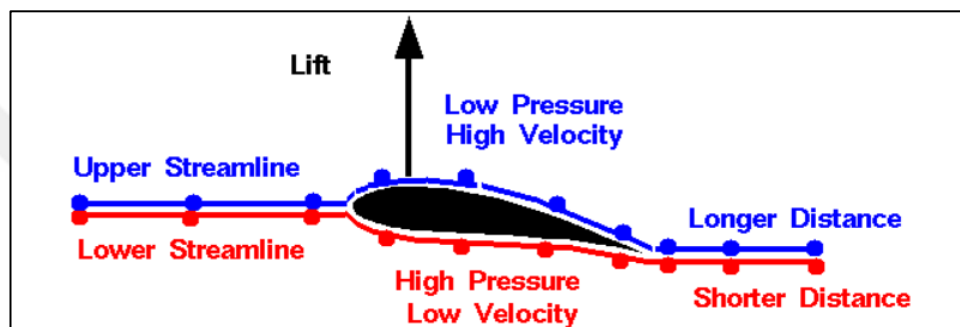


Figure 26: The Longer Path Theory

3.3. NUMERICAL SET-UP

Calculations are made using the CFD software ANSYS FLUENT code. The developed (SST) $k-\omega$ model was chosen to accurately predict airflows with strong reverse pressure gradients. The SST $k-\omega$ model is a two-equation model that accurately predicts pressure-dependent separation with a short calculation.

3.3.1. Test Matrix

In Table 3, test matrix is depicted. As it is seen in the Table, firstly radius of curvature ' V_1 ' is optimized with varying this value between $110 \text{ mm} < V_1 < 140 \text{ mm}$. After optimizing the V_1 , arc length ' V_2 ' is optimized with using the best scenario for V_1 . V_2 is varied between 20 mm to 40 mm.

Table 3: Test Matrix

Case	V_1	V_2	Figure
1	110 mm	40 mm	
2	120 mm		
3	125 mm		
4	130 mm		
5	135 mm		
6	140 mm		
7	130 mm	20 mm	
8		25 mm	
9		30 mm	
10		35 mm	
11		45 mm	

3.3.2. Boundary Condition

Choosing the appropriate boundary conditions is important for obtaining accurate results in CFD processes. As a boundary conditions, at the inlet of the UAV velocity inlet, at the outlet, pressure outlet and for the walls of the UAV, no slip boundary condition is utilized.

3.3.2.1. Velocity Inlet Condition

Boundary conditions at the velocity inlets are used to calculate the mass flow from the propeller inlet to the surface area. Energy, momentum and flow calculations are made through the inlet. The state of the flow entering the inlet and continuing along the surface is calculated in this section. When the flow entering the inlet is defined, the inlet mass flow rate, energy flows and momentum flows are calculated. The mass flow rate is calculated by the equation shown below:

$$\dot{m} = \int \rho \vec{V} \cdot d\vec{A} \quad (3.22)$$

3.3.2.2. Pressure Outlet Condition

For pressure outlet boundary conditions, gauge pressure should be displayed at the outlet boundary. The pressure shown can be subsonic or supersonic. Where the flow is supersonic, pressure will be observed from the internal flow. The surface pressure for incompressible flows is determined by averaging the given and internal pressure. P_f is face pressure can be calculated (P_c = Interior Cell Pressure, P_e = Exit Pressure):

$$P_f = 0,5(P_c + P_e) \quad (3.23)$$

3.3.2.3. Wall Condition

The flow rate is defined as zero at the walls. Pressure gradients are zero and the adiabatic boundary condition is given. All turbulence magnitudes are eliminated on the wall with the condition of non-slip.

3.3.3. Force Calculation

To obtain direct thrust and validation, control volume and linear momentum equation approach is utilized. In Figure 27, Control Volume and Linear momentum approach to calculating direct thrust of the Coanda Surface is depicted.

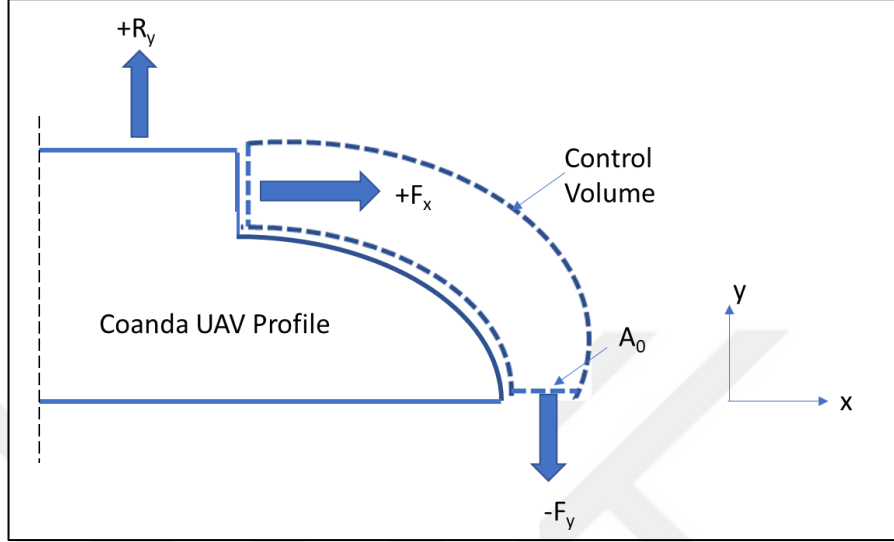


Figure 27: Control volume representation of UAV Profile

Due to the symmetry condition, forces acting on the x-axis cancel each other. The only leaving force is the -y forces. In sight of this, a reaction force is originated, which results in the craft ascent. As derived from the linear momentum direction, the equation to calculate direct thrust is thus:

$$F = \dot{m}V = (\rho \cdot A_{cs} \cdot V_y) \cdot V_y = \rho \cdot A_{cs} \cdot V_y^2 \quad (3.24)$$

A control surface denotes the surface area of the Coanda jet is leaving, V_y is the is the area-weighted average velocity in the y-direction of the Coanda jet. Fundamental conservation analysis will be applied to the control volume. The continuity equation:

$$V_{out} = \frac{\dot{m}}{2\pi\rho R_i h_i} = \frac{R_i h_i}{R_0 h_0} V_{in} \quad (3.25)$$

$$V_R = \frac{\dot{m}}{2\pi\rho R_i h_i} = \frac{R_i h_i}{R h_R} V_{in} \quad (3.26)$$

The contribution of the Coanda surface and momentum causes for differentiation of the momentum equation in the vertical (y) direction. The total lift force to be produced from the Coanda surface is equal to the sum of the vertical component of the momentum balance due to the Coanda effect and the pressure difference on the Coanda surface. The momentum equation in the y-direction for the control volume shown in Figure 28 is as follows since Momentum-In in the radial direction does not contribute to lift:

$$F_{CS} = \dot{m}V_{out} = 2\pi R_i h_i \rho V_{in} \cdot V_{out} \quad (3.27)$$

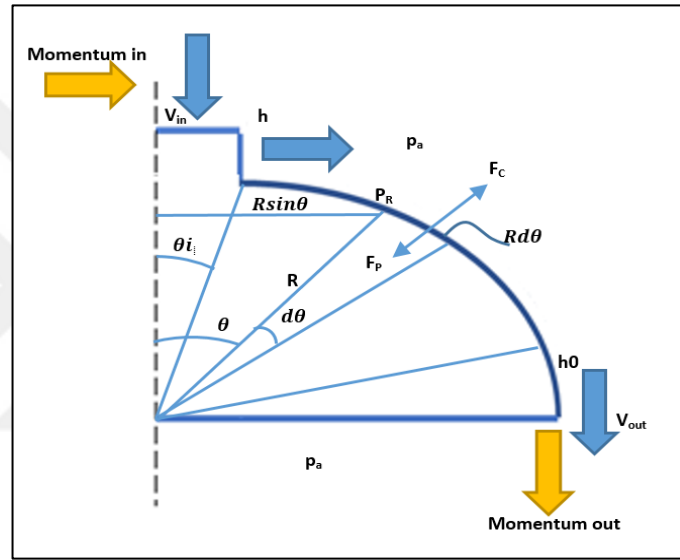


Figure 28: Control Volume of Coanda Model

The lift contribution caused by the pressure difference between the model's bottom and the curved Coanda surface is as follows:

$$F_{PD} = \pi(R_0^2 - R_i^2)p_a - \int_{\theta_i}^{\theta_0} \left(p_a - \frac{h}{R} \rho \left(\frac{\dot{m}}{2\pi\rho R h} \right)_R^2 \right) 2\pi R^2 \sin 2\theta d\theta \quad (3.28)$$

$$F_{PD} = \left(\frac{\dot{m}^2}{4\pi\rho h R} \right)_R \quad (3.29)$$

Based on these equations, considering the Coanda surface momentum and the pressure difference due to the Coanda surface, the total lift is found as:

$$Lift_{CS+PD} = 2\pi R_i h_i \rho V_{in} \times V_{out} + \left(\frac{\dot{m}^2}{4\pi\rho h R} \right)_R = \dot{m} \times V_{out} + \frac{1}{2} \dot{m} V_R \quad (3.30)$$

3.3.4. Structural Design

The ratio of maximum lift force and minimum friction force was compared among the parameters. ANSYS CFD module was used for flow analysis and simulations. CFD analyzes were performed in order to optimize the value of the two parameters. First, the analysis was prepared for increments of the radius of curvature, called V_1 parameter, between 110 mm and 140 mm. Then analyses have been performed made for the arc length, called V_2 parameter for constant V_1 . The optimum parameters have been selected according to the maximum C_L/C_D ratio of the analysis results.

There are some conditions about CFD. During the simulations, it is assumed that the environment is under standard temperature and pressure conditions. The formulation is "Implicit" and the kind of flux is "pressure based" in the CFD solution technique. Least square-based gradient calculations were used in the simulations. In order to examine the number effect on Reynold's flow behavior, inlet velocity $V= 3$ m/s, $V= 4$ m/s, $V= 5$ m/s velocities are used.

The viscosity model is set as "Turbulent". The $k-\omega$ SST turbulence model is used for modelling the turbulent flow. Because the two-dimensional profiles are symmetrical, centerline symmetry was used in the simulations to reduce on computing expenses. Velocity inlet, pressure outlet and wall boundaries are utilized. The radius of curvature was accepted as the wall condition, but it was named 'Coanda Surface' because it is the surface on which the Coanda effect will be observed. Boundary conditions and control volume are shown in Figure 29-30.

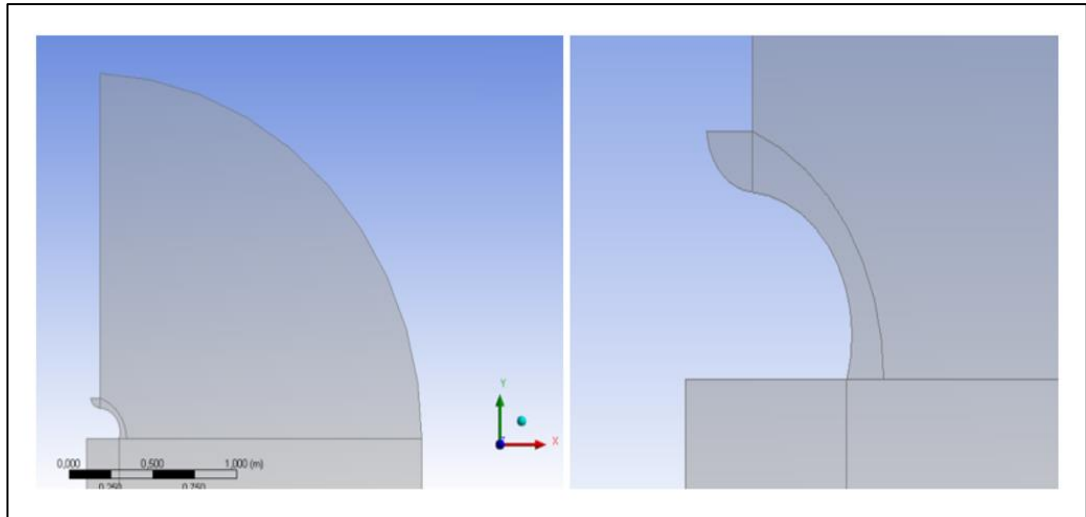


Figure 29: a) Fluent Area b) Model Geometry in Control Volume

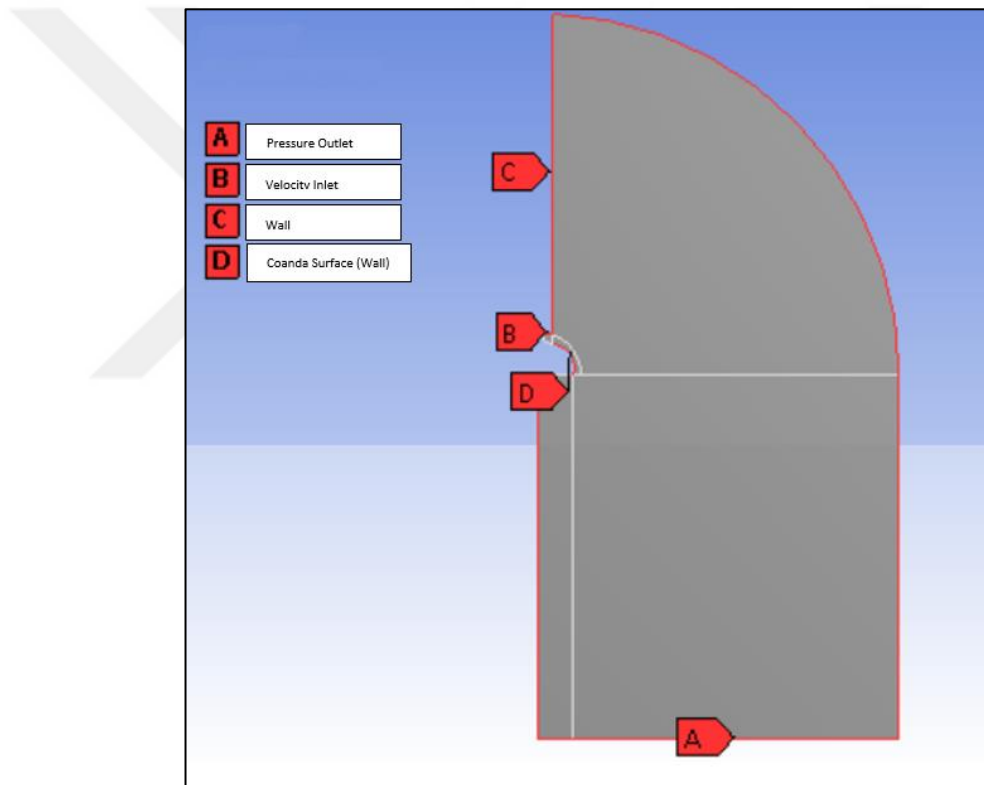


Figure 30: Boundary Conditions

Figure 31-34 shows the full meshed area applied for calculations. The total mesh rate varies in size and the structural mesh structure is utilized to the geometry. Inflation that is equal to 1 mm was utilized around to the inlet and Coanda surface where the flow behavior is critical. Since the fluid and the surface are in contact with the Coanda surface and the inlet, the inflation technique was used on these two surfaces as these are the critical flow region. This technique gives more accurate results as the fluid velocity changes as it approaches the surface. Mesh became increasingly tight and layered. While creating the flow area, a rectangular container was used. The part of the 5 m long, 2 m wide fluid container parallel to the oval surface of the model was made oval in the same way.

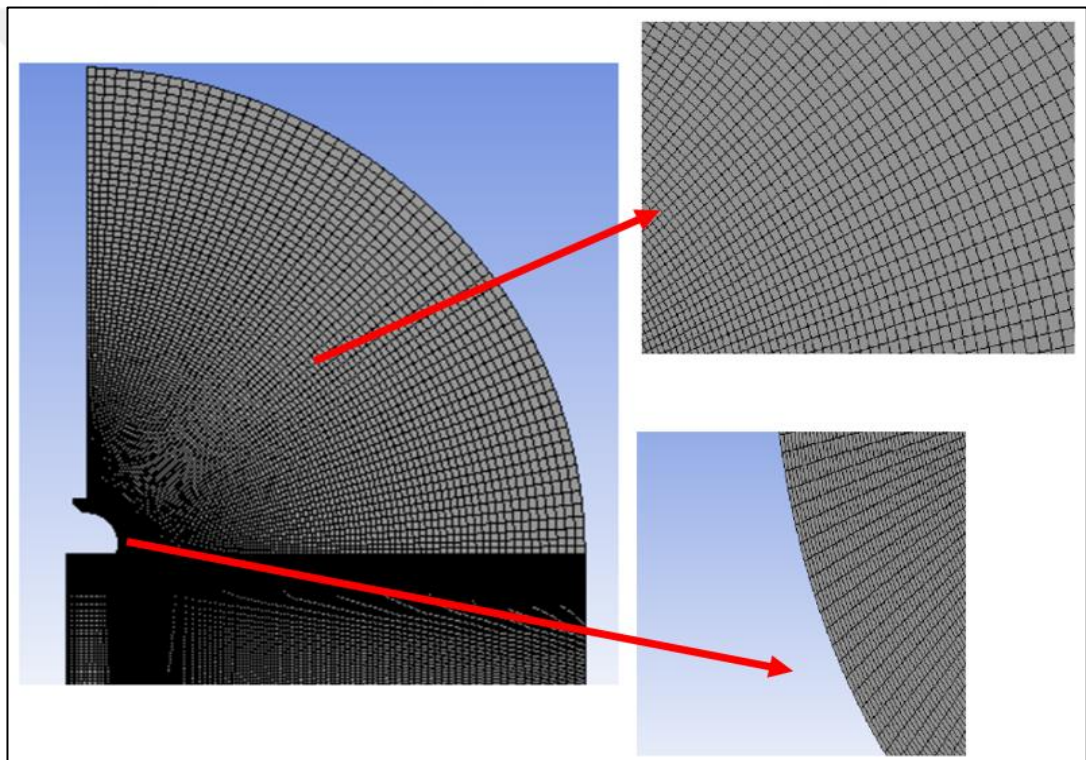


Figure 31. Mesh Domain

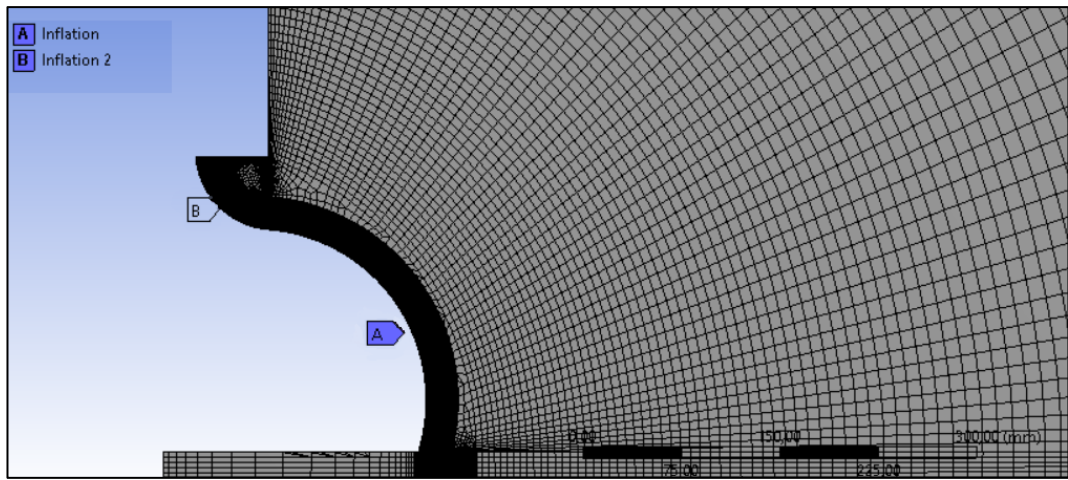


Figure 32: Inflation Geometries

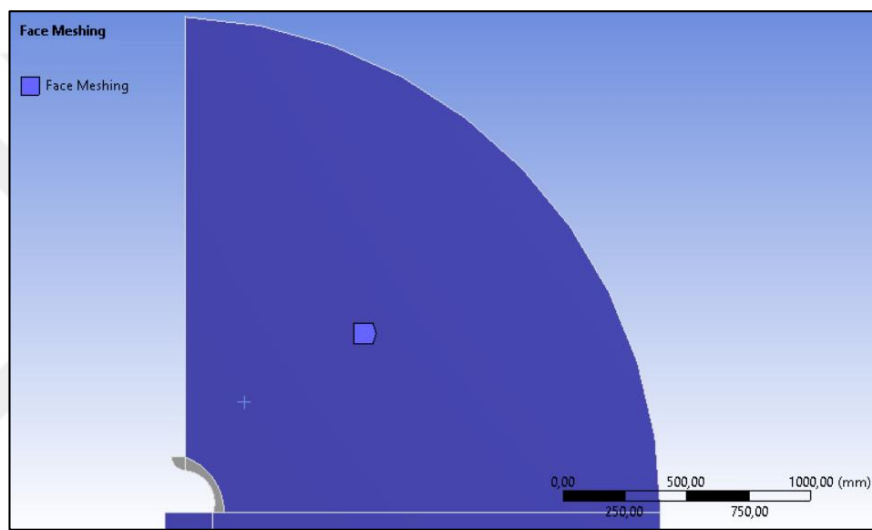


Figure 33: Face Meshing Areas

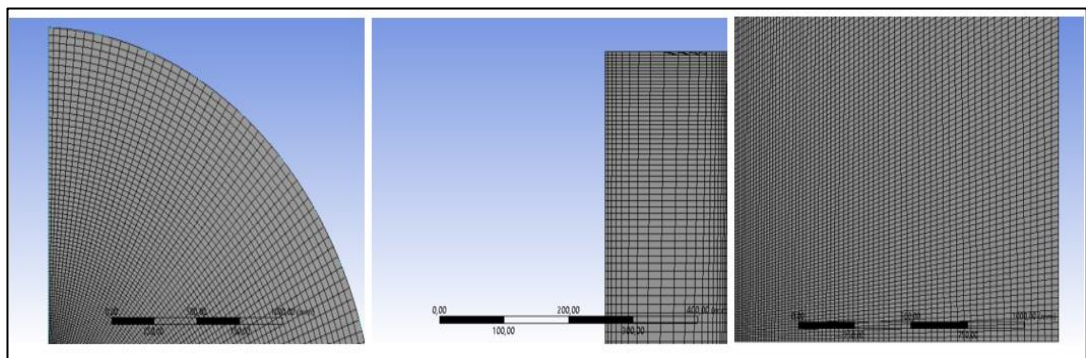


Figure 34: Face Meshing Geometry Details

3.3.5. Mesh Independency Study

A mesh independency study has been done for mesh verification. 5 different mesh structures are prepared for this study. As a control parameter lift force is chosen. When the lift force does not vary with the number of mesh, that means the results become independent from the mesh. The value 75×10^4 is chosen as the limit value. After this interval, the average errors of the variables remain below 1%. Therefore, also thinking the computational cost, after that point the mesh with 750.000 element will be used.

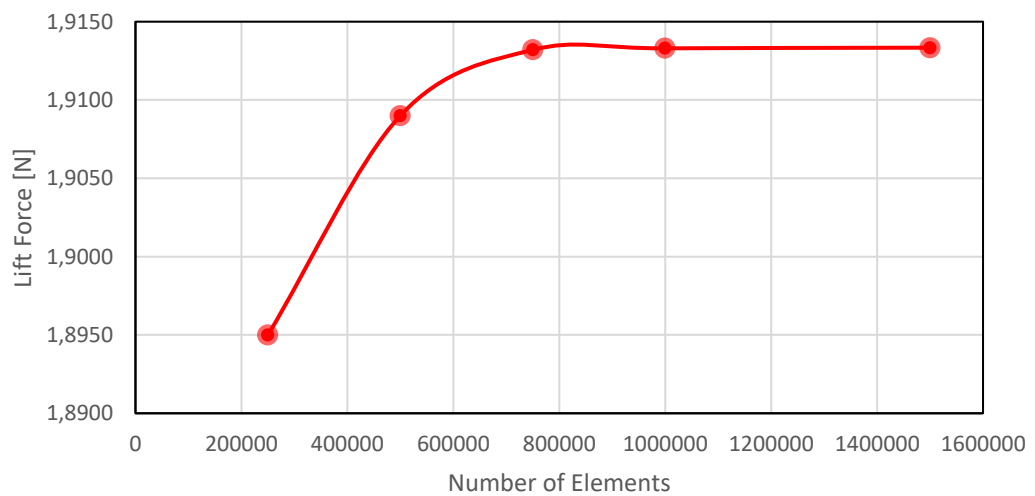


Figure 35. Mesh Independency Study

3.3.6. Validation Study

Validation of the numerical study is performed in two ways. First way is the using of Bernoulli equation method. As explained in detail in the 1.3. Coanda Effect, according to Bernoulli's Theorem, the pressure gradient, $\partial p/\partial n$, is exactly proportional to the fluid density times the square of the fluid velocity divided by the radius of curvature of the streamline. It has been observed that the pressure gradients obtained from the simulations are similar to the results calculated according to the Bernoulli theorem applied to the streamline in the normal direction. Also, as a second method empirical relationship is used that predicts the separation angle.

3.3.6.1. Pressure Gradient Estimation with Bernoulli Equation

As a first validation method, pressure change across to the normal direction is estimated and compared with the Bernoulli theorem as given in Eq (3.25).

$$\frac{\partial p}{\partial n} = \rho \frac{v^2}{R} \quad (3.25)$$

This equation indicates that, pressure change through the normal direction is function of the square of the free stream velocity, air density and inversely proportional to the radius of the curvature as shown in Figure 36. For constant separation angle of 30° , theoretical and numerical pressure variation distribution through the height/radius of curvature (h/R) is obtained as it is given in Figure 36. As it is illustrated in Figure 36, the maximum difference between the theoretical and numerical study is only 6.7%.

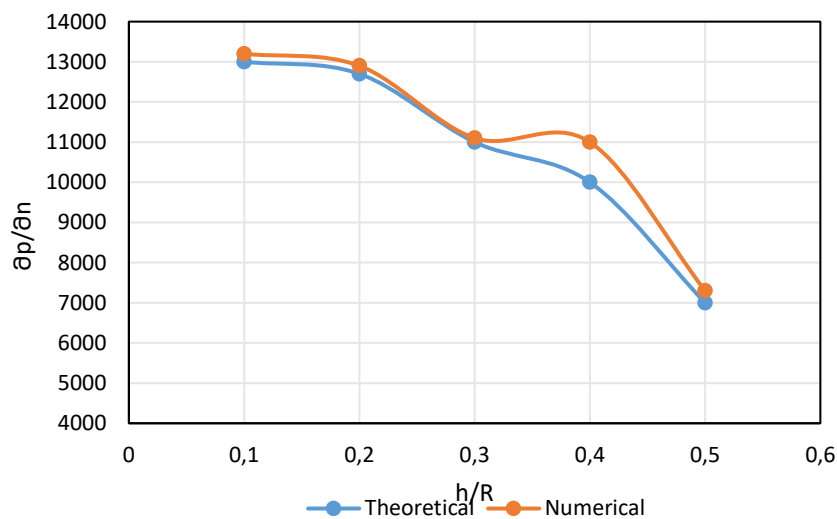


Figure 36: Validation study regarding to Bernoulli Equation

3.3.6.2. Separation Angle Estimation using the Empirical Relationship

Dragan [33], derived a mathematical model for high thickness Coanda effect wall jets as given in Eq 3.26, by using the Sleeman- Phelps equation [38].

$$\theta_{separation} = 6.69 \left(\frac{R}{h}\right)^{1.54} \quad (3.26)$$

As a validation method Eq 3.26 is used and separation angle is calculated for numerical study and with using the empirical relationship. For orifice height $h=30$ mm and for R as a radius of curvature (V_1) value varying between $110 \text{ mm} < R < 140 \text{ mm}$ separation angle is calculated and compared with the empirical relationship. The maximum deviation is 9.51%.

Table 4: Comparison of numerical results with the empirical correlation [34]

h (mm)	R (mm)	Empirical Separation Angle	Numerical Separation Angle	% Difference
30	110	49,48	53,57	8,27
30	120	56,57	59,254	4,74
30	130	63,99	66,254	3,53
30	140	71,73	78,548	9,51

Regarding to the validation study maximum error is calculated as 9.51%. As results are compatible with each other, it can be said that, developed numerical methodology is accurate and can be used in the geometrical optimization of the UAV Coanda.

3.3.6.3. Turbulence Model Study

The ability of $k-\epsilon$, $k-\omega$, and $k-\omega$ SST turbulence models in the prediction pressure distribution through the normal surface of the UAV is examined in this part of the study. One of the most popular models for capturing the impact of turbulent flow conditions is the $k-\omega$ SST turbulence model. In comparison to most RANS models, the $k-\omega$ SST model offers a superior forecast of flow separation and also explains its good behavior in the presence of negative pressure gradients. It has the ability how the main shear stress moves through boundary layers with negative pressure gradients. Due to its excellent accuracy to expense ratio, it is the type that is most frequently utilized in the industry [39-41].

Those three turbulence models are used in order to solve the flow field through the UAV. According to the results, $k-\omega$ SST turbulence model gives best prediction when it is compared to the other two turbulence models. Especially, $k-\epsilon$ turbulence models' prediction power is lower than the other two models and it over-predicts the pressure distribution.

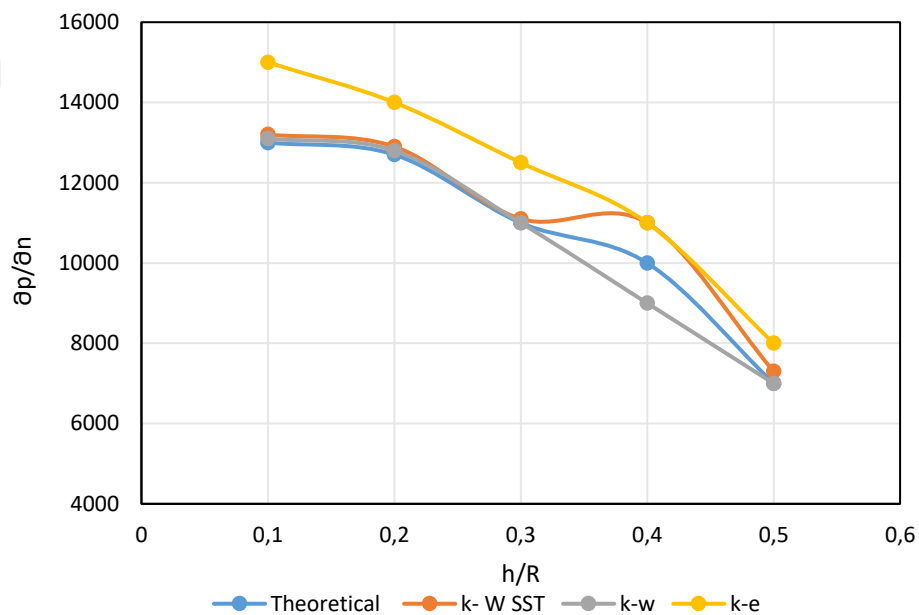


Figure 37: Turbulence model study

CHAPTER IV

RESULTS

Here, CFD simulations were created using ANSYS Fluent to evaluate the results. The results are simulated using the two-equation RANS model. The $k-\omega$ Shear Stress Transport (SST) turbulence model was chosen. CFD analyses are performed in order to optima the value of V_1 (radius of curvature) and V_2 (arc length) parameters. The effects of both parameters on performance were examined separately. The values obtained from the input speed of 4 m/s were compared. Lift and drag forces, and lift and drag coefficients were obtained. Velocity contour graphics were drawn. It was observed whether the flow would separate from the surface before or after the separation angle. When the results of the analysis are examined, it is desired that the drag force decreases while the lift force increases. In this context, choosing the optimum surface parameter with the C_L/C_D ratio was decided. In Figure 38, Surface variables used in the CFD analysis is depicted. After optimizing the geometry of the Coanda, effect of the free stream velocity on the flow behavior is also investigated.

A high C_L/C_D ratio is obtained when $V_1=110$ mm between the parameters. However, it was eliminated because the lift force could not be obtained at this value. The value that creates the lifting force and obtains a high C_L/C_D ratio is $V_1=130$ mm.

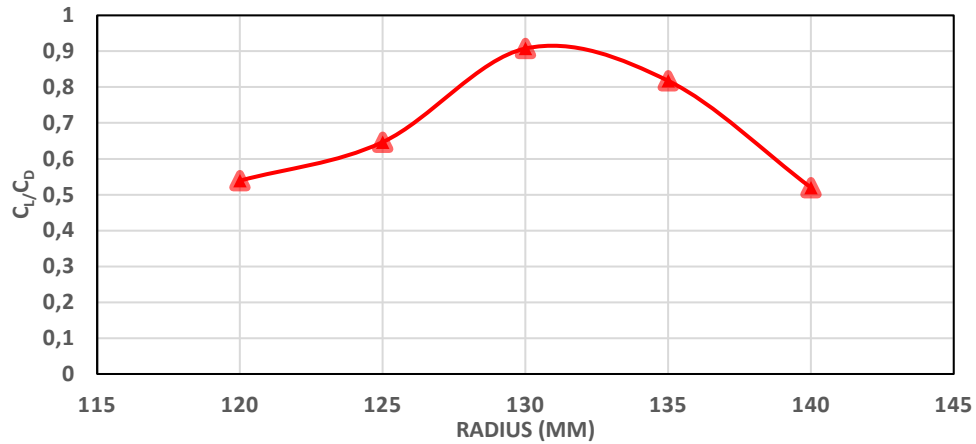


Figure 39: Rate of C_L/C_D Over Variable V_1 Values

The results of comparing the C_L/C_D ratio variation through h/R is depicted in Figure 22. It was that the there is a critical h/R value, before reaching to that critical point the C_L/C_D increases and after reaching to the critical value, ratio starts to decreases. It was observed that for this geometrical configuration h/R_{Critical} is= 0.34 mm.

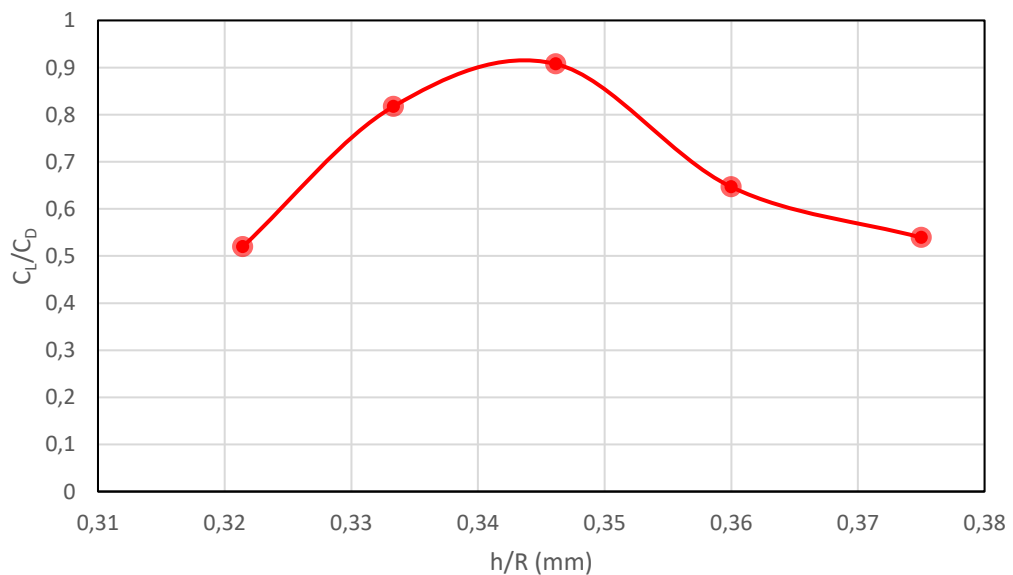


Figure 40: Comparison of C_L/C_D Over h/R

4.1.2. Velocity Contours of V_1 Parameters

In Figure 41, velocity contours for the geometries with the different radius of curvature is depicted. On the upper surface of the UAV pressure decreases and velocity increases gradually. Towards the edge of the upper part, suction force is created which produces upward net force, keeps the UAV in hovering. Before reaching to the critical V_1 value ($V_1=130\text{mm}$), flow cannot be stay attached to the surface and early separation is observed. At the critical point, where lift force reaches to its maximum value, Coanda effect is strongly observed and late separation is obtained. When the curvature radius is increased too much no separation is observed and fluid flows through to the surface.

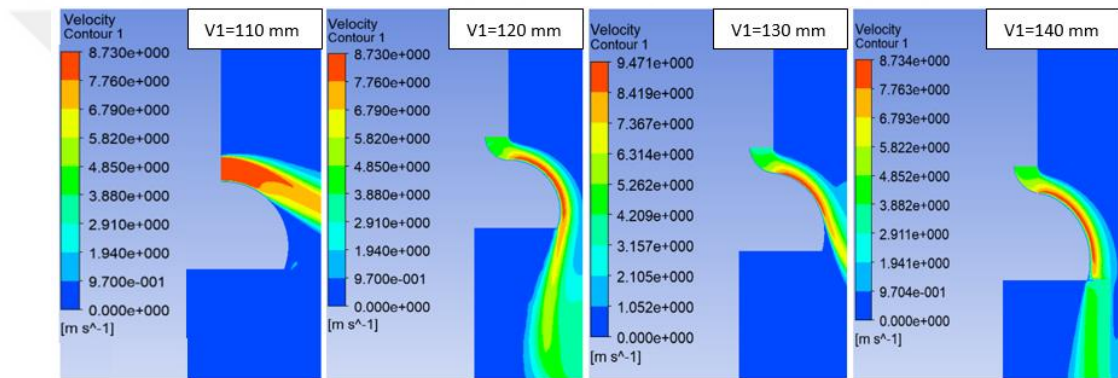


Figure 41: Velocity Contours for a) $V_1=110$ mm b) $V_1=120$ mm c) $V_1=130$ mm d) $V_1=140$ mm

In Table 6, θ_s angles are given according to C_L/C_D ratios. Here, the separation angle is taken into account depending on the radius of curvature. The separation angle at which the maximum C_L/C_D ratio is observed is $\theta_s = 22^\circ$ when radius of curvature $R=130$ mm.

Table 6: V_1 Parameters Analysis Results

Test Number	V_1	V_2	Lift Coefficient	Drag Coefficient	C_L/C_D	h/R	Separation Angle θ_s
1	110 mm	40 mm	0,57	0,20	2,79	0,41	39°
4	130 mm		1,91	2,10	0,90	0,34	22°
6	140 mm		1,66	3,07	0,51	0,32	0°

To predict the separation angle Eq (11) is used. As it is shown in Fig. 42, when $V_1 = 110$ mm, θ_s is calculated as 39° and, and when $V_1 = 140$ mm, θ_s is calculated as 0° . Results indicate that, with increasing the radius of curvature, separation angle value decreases.

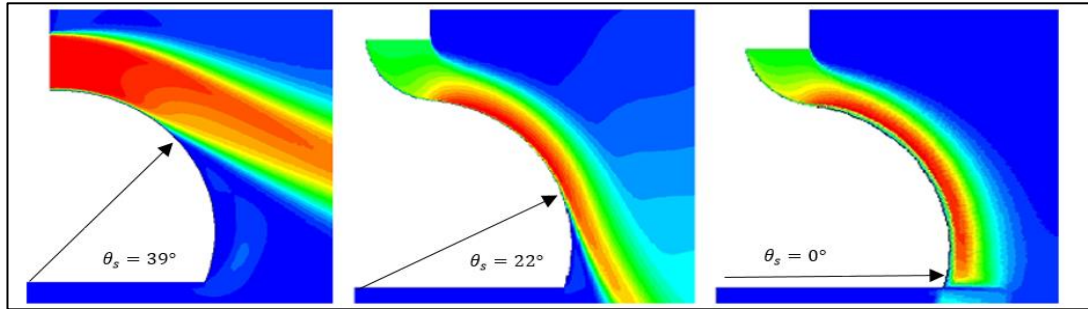


Figure 42: a) Early Separation b) Optimal Separation c) No Separation

According to the results, it is seen that directing the flow over a Coanda surface negative pressure zone is generated and addition lift is gained. With the separation angle of 22° , where separation is observed through the rear edge of the Coanda surface, maximum lift is created. When fluid is stick to the Coanda surface with no separation ($\theta_s = 0^\circ$), lift is decreased. In sight of this situation, it can be claimed that, separation position should be optimized in order to maximize the lift coefficient. For the under investigated geometry optimized $V_1 = 130$ mm.

4.2. INVESTIGATION OF THE V_2 EFFECT ON PERFORMANCE

After simulations of V_1 parameters, $V_1=130$ mm was chosen. According to this analysis, simulations of V_2 parameters that directly affect the lift were prepared. In this section, parameter analyzes were made that allow the flow through the surface to be separated after providing the maximum lift. As in the analysis of V_1 parameters, the maximum C_L/C_D ratio was considered. V_2 analyzes were carried out by keeping $V_1=130$ mm constant in the model.

Table 7: V_2 Parameters

V_1	V_2	Lift Coefficient	Drag Coefficient	Lift Force (N)	Drag Force (N)	C_L/C_D
130 mm	20 mm	1,67	2,75	1,02	1,68	0,606087
	25 mm	1,66	2,88	1,02	1,68	0,577621
	30 mm	1,60	2,93	0,98	1,79	0,54684
	35 mm	1,61	3,12	0,98	1,91	0,515907
	40 mm	1,91	2,10	1,17	1,29	0,907547
	45 mm	1,50	3,23	0,92	0,98	0,46557

The C_L/C_D distribution for different arc lengths is shown in Figure 43. The maximum C_L/C_D ratio was obtained when $V_2=40$ mm.

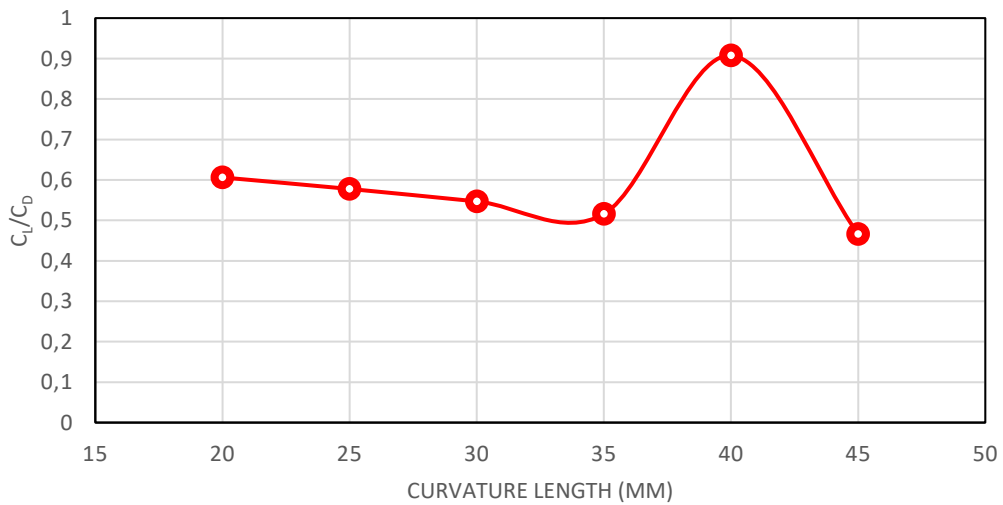


Figure 43: Rate of C_L/C_D Over V_2

4.2.1. Velocity Contours of V_2 Parameters

As shown in the figure below, the V_2 parameter has a direct relationship to the V_1 parameter and directly affects the lift. In this analysis, the effect of V_2 parameters, which is defined as the arc length, which is effective in the separation of the flow from the surface, on the separation was observed. $V_2=40$ mm corresponds to the maximum C_L/C_D ratio taken from the active Coanda surface.

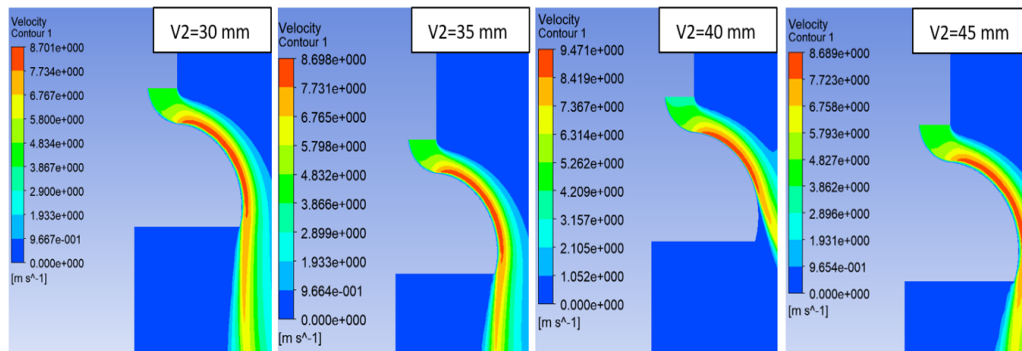


Figure 44: Velocity Contours Graphs a) $V_2=30$ mm b) $V_2=35$ mm c) $V_2=40$ mm d) $V_2=45$ mm

As shown in Figure 44., the following two results were observed:

- The flow is not separated from the surface before reaching to the critical curvature length.
- The flow is separated from the surface at the critical V_2 value.

4.3. UAV PERFORMANCE UNDER DIFFERENT REYNOLDS NUMBERS

For the UAV geometry with $V_1 = 130$ mm and $V_2 = 40$ mm, free stream velocity is varied between $4 \text{ m/s} < u_\infty < 6 \text{ m/s}$. As shown in Figure 45, the lift coefficient rises sharply as h/R is low, peaking around R_{critical} then drops. This increment and drastical reduce is caused by the Coanda jet separating from the Coanda surface as shown in the Figure 45. It should be noted that separation angle has a direct effect on the C_L/C_D ratio. The trend of the lift to drag ratio is similar to each other for all of the Reynolds number. The only difference is increment in the free stream velocity value causes rise in the C_L/C_D ratio.

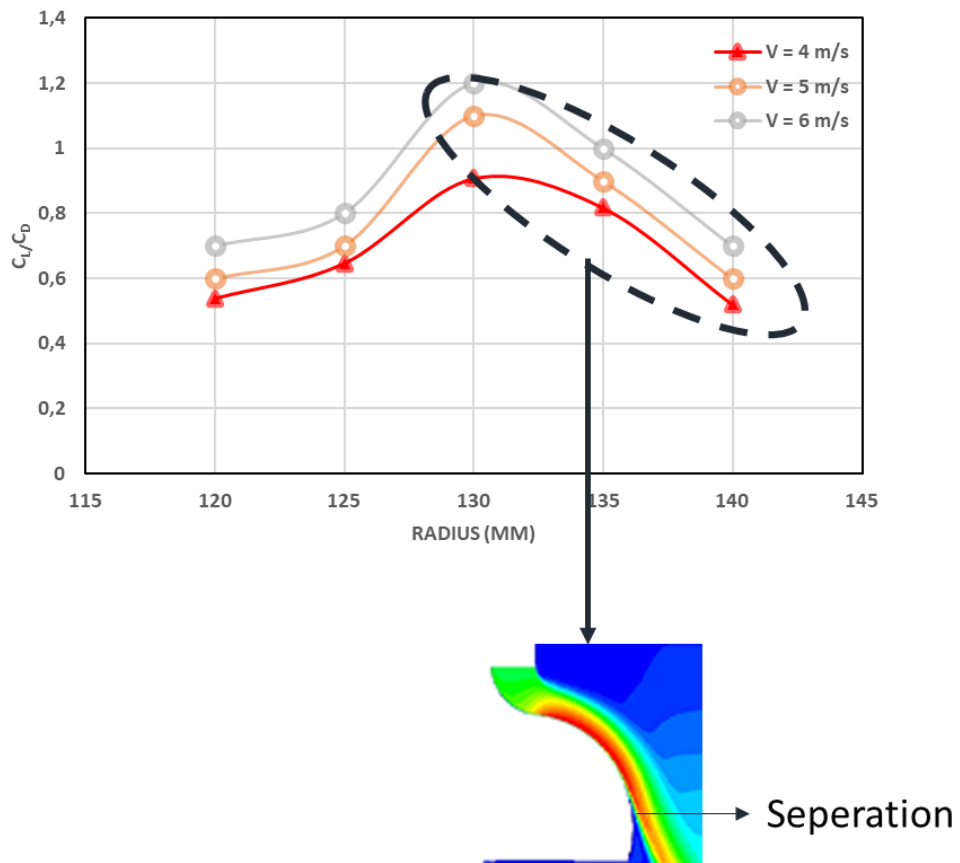


Figure 45: Velocity Performance According to C_L/C_D vs Radius

4.4. FLOW BEHAVIOR INVESTIGATION FOR THE BEST CASE

The effects of radius of curvature V_1 and arc length V_2 parameters on aerodynamic performance were found using CFD simulation. The velocity magnitude contours according to $V_1=130$ mm and $V_2=40$ mm are presented below. The main reason for the fluid to adhere to the surface is that the contact pressure is lower than the ambient pressure due to viscous entrainment. With such viscous flows, the average velocity decreases as the surface pressure increases. This finding is also proven by the velocity and pressure contour charts below.

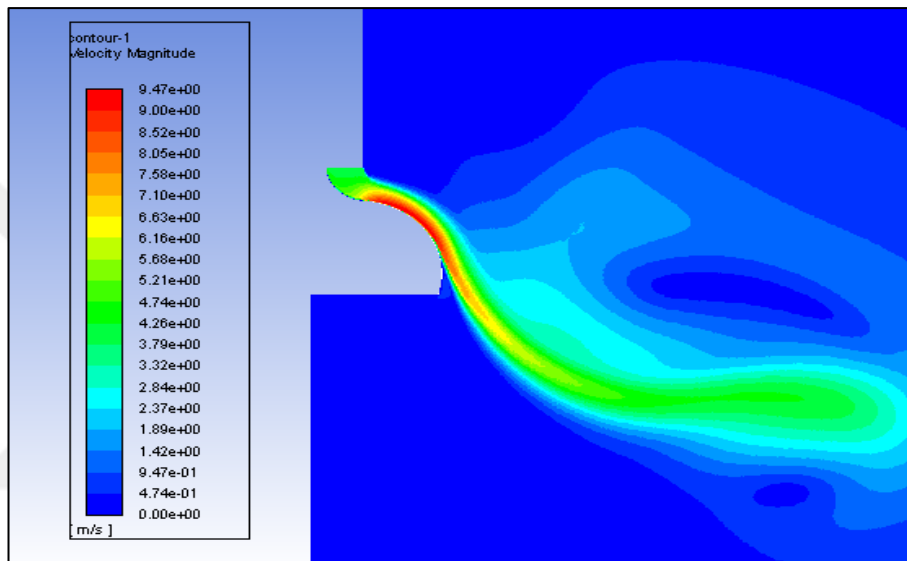


Figure 46: Velocity Magnitude Contour

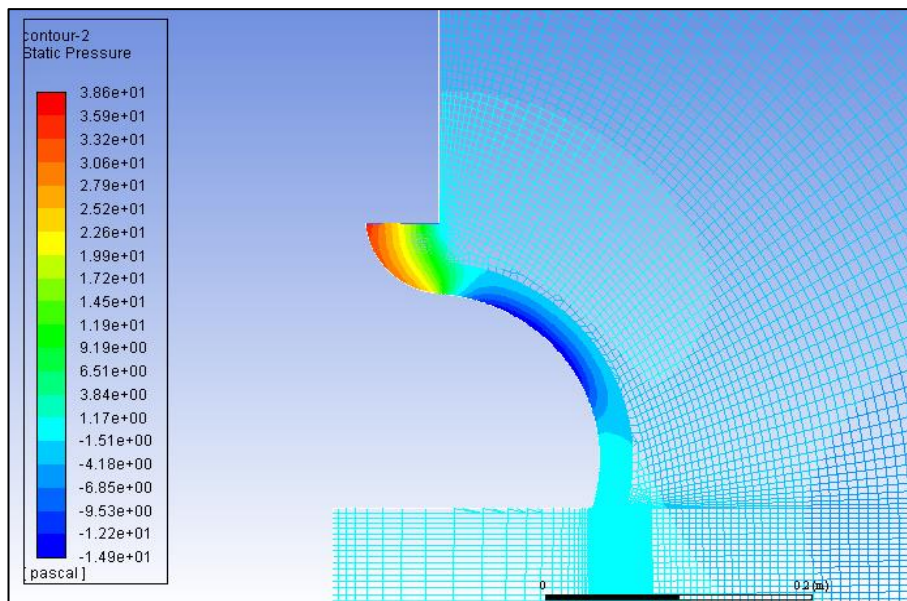


Figure 47: Static Pressure Contour

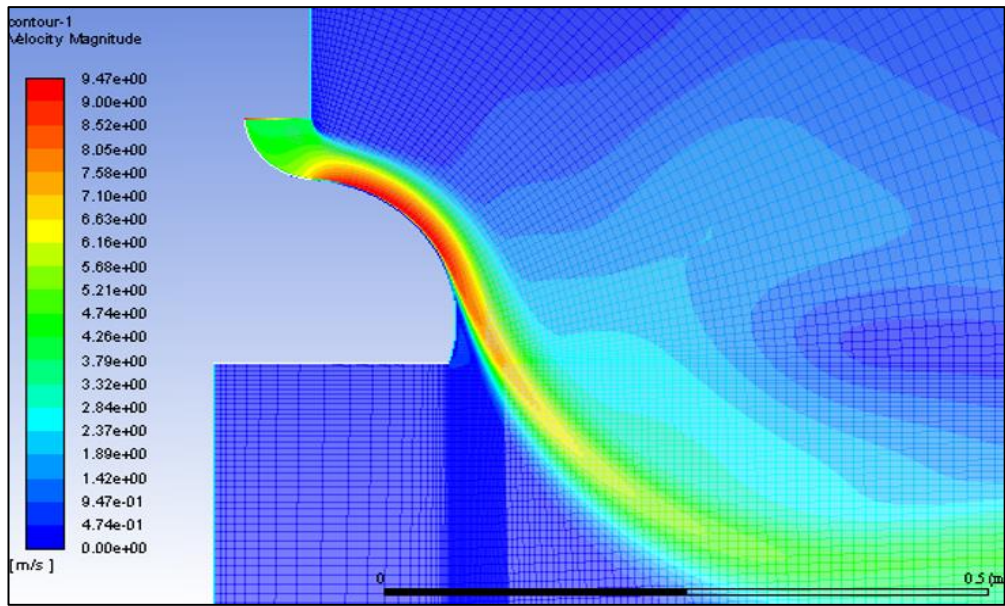


Figure 48: Velocity Contour

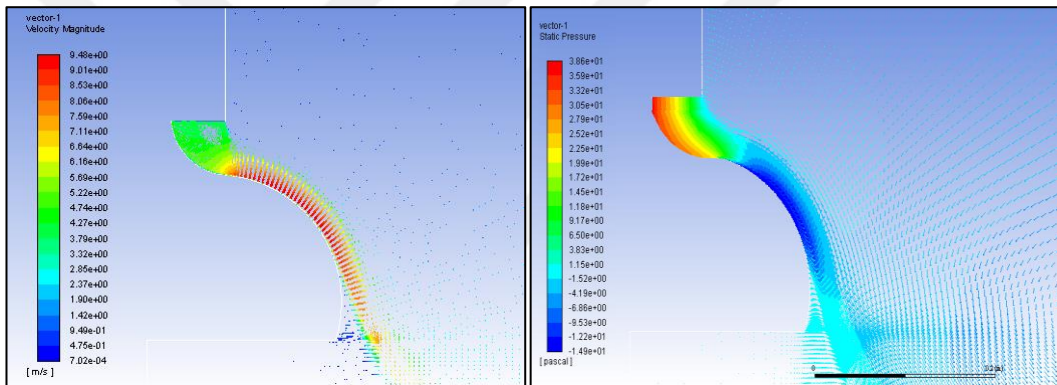


Figure 49: Velocity Magnitude and Static Pressure Vectors

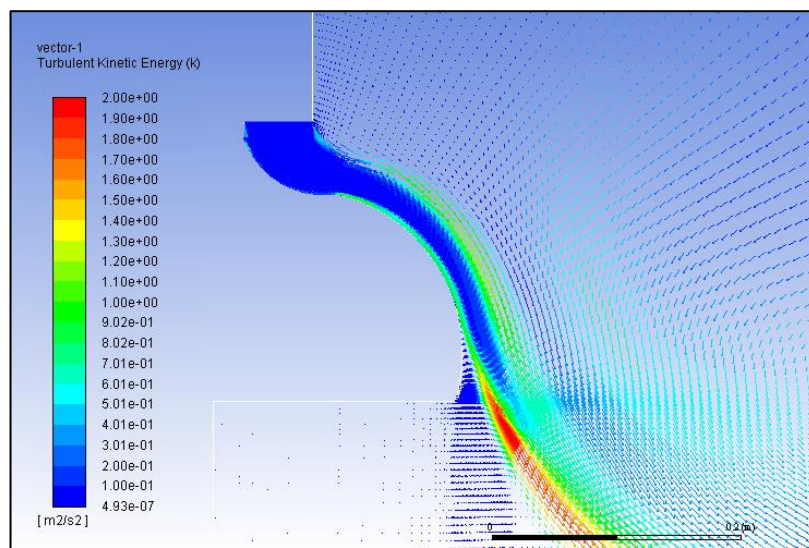


Figure 50: Turbulent Kinetic Energy Vector

CHAPTER V

CONCLUSION

In this thesis, the effect of the Coanda effect on lift and drag coefficients was observed using the computational fluid dynamics software ANSYS Fluent® when various design parameters and velocity values were changed. Three-dimensional models were made parametrically using Autodesk Inventor program. The simulations were performed with modelling the RANS equations with k- ω SST turbulence model. For verification, pressure distribution through the Coanda surface is obtained with using the Bernoulli equation and as a second method validation is performed with using the empirical equation in the literature that predicts the flow separation angle. Analyzes were carried out with using different radius of curvature and different arc lengths. The effects of these parameters on performance were examined. Lift-drag coefficient and lift-drag force values were found. Values found with CFD simulations were compared, velocity contour graphs were created. The h/R and C_L/C_D ratios were compared to determine the optimum surface parameters. According to these results, the optimum radius of curvature and arc length were found. These results are accepted as the surface parameters that will increase the thrust/lift force in the Coanda-effect UAV design.

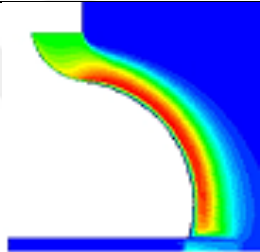
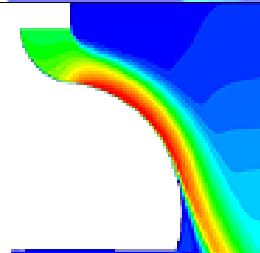
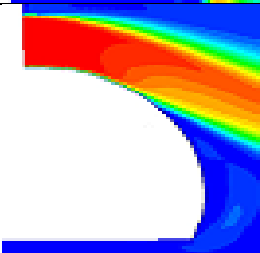
According to the simulation results, graphs based on the C_L/C_D ratio were obtained. The parameter that creates the maximum C_L/C_D ratio and leaves after creating lift on the active Coanda surface is $V_1=130$ mm and $V_2=40$ mm.

According to theoretical studies, it is accepted that reducing the radius of curvature after reaching to a critical point increases the lifting force [40]. Insight of the results obtained from the CFD simulations, the parameter V_1 referred to as the radius of curvature reaches a critical level when it is 130 mm. It is seen that the lift force decreases with increasing of this value.

At the same time, another parameter affecting the C_L/C_D ratio is the ratio of orifice height h and radius of curvature V_1 . It is seen that as h/R increases, the C_L/C_D coefficient decreases. This reduces the Coanda surface area, which creates a lifting effect. As the h/R ratio increases, the separation angle also increases. In this part, the maximum C_L/C_D value is observed in cases where the h/R ratio ($0.30 < h/R < 0.35$) is present.

Table 8 compares the values found from the equations estimating the separation angle with the velocity contours obtained from the ANSYS Fluent module. When the flow separation angle defined in Table 8 and the resulting velocity contours are compared, it is observed that there are results close to the theoretically calculated value. Studies on the separation angle of a curved Coanda wall jet of $h/R > 0.10$ were validated [33].

Table 8: Flow Separation Estimation

h/R	θ_s	Velocity Contour
0,32	0°	
0,34	22°	
0,41	39°	

REFERENCES

- [1] CHRISTOPHER Chant (1978), *Aviation: An Illustrated History*, Chartwell Books, USA.
- [2] ACKROYD, J. A. D. (2002), “Sir George Cayley, the father of aeronautics. Part 1. The invention of the aeroplane.”, *Notes and Records of the Royal Society of London*, 56.2: 167-181.
- [3] GIBBS-SMITH Charles Harvard, et al. (1962), *Sir George Cayley's Aeronautics, 1796-1855*, HM Stationery Office, London.
- [4] GIBBS-SMITH Charles Harvard (1962), “Father of aerial navigation”, *Notes and Records of The Royal Society of London*, vol. 17, No. 1, p. 36-56.
- [5] ACKROYD J.A.D. (2011), “Sir George Cayley: The invention of the aeroplane near Scarborough at the time of Trafalgar.”, *Journal of Aeronautical History Paper*, No. 6.
- [6] HARVARD Charles Gibbs Smith (2003), *Aviation*, Science Museum, London.
- [7] KÉITH LUCAS David (1965), The Life of a Genius: Sir George Cayley, pioneer of modern aviation. G. Fairlie and E. Cayley. Hodder and Stoughton, London, 191 p. 25s.,” *The Journal of the Royal Aeronautical Society*, vol. 69, No. 660, pp. 881–881.
- [8] LILIENTHAL Otto (1896), Practical experiments for the development of human flight, *The Aeronautical Annual*, 7-20.
- [9] STOESSEL Rainer, et al. (2018), “Computed Tomography testing at remains of a glider from Otto Lilienthal.”, In, *8th Conference on Industrial Computed Tomography*, Wels, Austria.
- [10] LUKASCH Bernd (2003), From Lilienthal to the Wrights, *Otto-Lilienthal-Museum Anklam*.
- [11] JAKAB Peter L. (1996), *Visions of a Flying Machine: The Wright Brothers and the process of invention*, Smithsonian Institution, USA.
DOI: 10.1604/9781560987482.
- [12] PADFIELD Gareth D., LAWRENCE Ben (2003), “The birth of flight control: An engineering analysis of the Wright Brothers’ 1902 glider.”, *The Aeronautical Journal*, vol. 107, No. 1078, p. 697-718.
DOI: 10.1017/s0001924000013464.

- [13] WRIGHT Orville & Wilbur (1906), *Flying Machine*, U.S. Patent No. 821 393, United States Patent Office.
- [14] YOUNG Thomas (1800), “VII. Outlines of experiments and inquiries respecting sound and light. By Thomas Young, M. D. F. R. S. in a letter to Edward Whitaker Gray, M. D. Sec. R. S.”, *Philosophical Transactions of the Royal Society of London*, vol. 90, p. 106–150.
- [15] COANDA Henry M. (1936), *Device for deflecting a stream of elastic fluid projected into an elastic fluid*, U.S. Patent No. 2,052,869, United States Patent Office.
- [16] NEDELICUT Florin (2010), “Coanda effect UAV-a new born baby in the unmanned aerial vehicles family.”, *Review of the Air Force Academy*, 2:21.
- [17] COANDA Henry M. (1936), *Lifting Device Coanda Effect*, U.S. Patent No. 3,261,162, United States Patent Office.
- [18] NEWMAN B. G. (1961), “The deflection of plane jets by adjacent boundaries-Coanda effect.”, *Boundary layer and flow control*.
- [19] CARPENTER, P. W., and GREEN, P. N. (1997), “The Aeroacoustics and Aerodynamics of High-Speed Coanda Devices, Part 1: Conventional Arrangement of Exit Nozzle and Surface”, *Journal of Sound and Vibration*, Vol. 208, No. 5, p. 777-801.
- [20] BRADSHAW Peter (1973), *Effects of streamline curvature on turbulent flow*, ADVISORY GROUP FOR AEROSPACE RESEARCH AND DEVELOPMENT PARIS (FRANCE).
- [21] ZHOU Yaoming, et al. (2020), “An evaluative review of the VTOL technologies for unmanned and manned aerial vehicles.”, *Computer Communications*, v 149, p 356-369.
- [22] COANDA Henry M. (1938), *Propelling Device*, U.S. Patent No. 2,108,652, United States Patent Office.
- [23] NEDELICUT Florin (2010), “Towards a new class of aerial vehicles using the coanda effect.”.
- [24] COLLINS Robert Jhon (2003), *Aerial Flying Device*, U.K. No. GB 2,387,158, United Kingdom Patent Office.
- [25] DAY Terry (2008), “The Coanda effect and lift.”, *New Fluid Technology*.
- [26] HATTON G., MCINTOSH S. (2005), *Craft having flow-producing rotor and gyroscopic stability*, U.K. No. GB 2.424: 405, United Kingdom Patent Office.

- [27] NAUDIN Jean Louise (2006), "The GFS UAV Project.", *Retrieved on*, 25:2010.
- [28] NEDELICUT Florin, CONSTANTINESCU Sorin-Gabriel (2011), "LUAV's are the right approach for surveillance civil missions.", In, *International Conference of Scientific Paper AFASES*, p. 1237-1240.
- [29] CRIVOI Ovidiu, et al. (2013), "A survey of unmanned aerial vehicles based on Coanda effect.", *Thenomus Ji*, 20.
- [30] BENNER S.D. (1964), "The Coanda effect at deflection surfaces widely separated from the jet nozzle.", *University of Toronto, UTISA Technical Note*, No. 78.
- [31] MIRKOV Nikola, RASUO Bosko (2010), "Numerical simulation of air jet attachment to convex walls and applications.", In, *Proceedings of 27th International Congress of the Aeronautical Sciences-ICAS*.
- [32] SCHROIJEN Marcel, VAN TOOREN Michel (2009), "Mav propulsion system using the coanda effect.", In, *45th AIAA/ASME/SAE/ASEE Joint Propulsion Conference & Exhibit*, p. 4809.
- [33] DRAGAN Valeriu (2013), "A new mathematical model for high thickness Coanda effect wall jets.", *Review of the Air Force Academy*, 1: 23.
- [34] WEESAPAKDEE Baramee, et al. (2014), "An experimental and computational fluid dynamic study of axis-symmetric Coanda configuration for VTOL MAV applications.", In, *Applied Mechanics and Materials*, p. 42-47, Trans Tech Publications Ltd.
- [35] FLORESCU Daniela, et al. (2010), "Fuselage Airstream Simulation for a Coandă UAV.", *Review of the Air Force Academy*, 17.2: 83-88.
- [36] MENTER FLORIAN R. (1993), "Zonal two equation $k-\omega$ turbulence models for aerodynamic flows.", In, *23rd fluid dynamics, plasmadynamics, and lasers conference*, p. 2906.
- [37] JOHNSON W., SILVA C. (2022), "NASA concept vehicles and the engineering of advanced air mobility aircraft.", *The Aeronautical Journal*, 126.1295: 59-91.
- [38] YEN K. T. (1982), "An Analysis of the Flow Turning Characteristics of Upper-Surface Blowing Devices for STOL Aircraft.", PENNSYLVANIA STATE UNIV KING OF PRUSSIA KING OF PRUSSIA CENTER.
- [39] YU Chao, et al. (2018), "Heat exchange performance optimization of a wheel loader cooling system based on computational fluid dynamic simulation.", *Advances in Mechanical Engineering*, 10.11: 1687814018803984.

- [40] CATALANO Pietro, AMATO Marcello (2003), “An evaluation of RANS turbulence modelling for aerodynamic applications.”, *Aerospace science and Technology*, 7.7: 493-509.
- [41] MANZARI, M. T., et al. (1998), “Turbulent flow computations on 3D unstructured grids.”, *Finite elements in analysis and design*, 30.4: 353-363.
- [42] AUSTIN Reg (2011), *Unmanned aircraft systems: UAVS design, development and deployment*, John Wiley & Sons, United Kingdom.
- [43] DUMITRACHE A., et al. (2012), “Mathematical modelling and numerical investigations on the Coanda effect.”, *Nonlinearity, Bifurcation and Chaos-Theory and Applications*, 101-132.
- [44] LEE Hyunyong, et al. (2017), “Design optimization, modeling, and control of unmanned aerial vehicle lifted by Coandă effect.” *IEEE/ASME Transactions on Mechatronics*, 22.3: 1327-1336.
- [45] DOJODIHARDJO Harijono, et al. (2017), “First principle analysis of Coandă micro air vehicle aerodynamic forces for preliminary sizing.” *Aircraft Engineering and Aerospace Technology*.